



Two-stage partial melting during the Variscan extensional tectonics (Montagne Noire, France)

Marc Poujol, Pavel Pitra, Jean van den Driessche, Gilles Ruffet, Romain Tartèse, Jean-Louis Paquette, Jean-Charles Poilvet

► To cite this version:

Marc Poujol, Pavel Pitra, Jean van den Driessche, Gilles Ruffet, Romain Tartèse, et al.. Two-stage partial melting during the Variscan extensional tectonics (Montagne Noire, France). *International Journal of Earth Sciences*, 2017, 106 (2), pp.477-500. 10.1007/s00531-016-1369-1 . insu-01341984

HAL Id: insu-01341984

<https://insu.hal.science/insu-01341984>

Submitted on 11 Jul 2016

HAL is a multi-disciplinary open access archive for the deposit and dissemination of scientific research documents, whether they are published or not. The documents may come from teaching and research institutions in France or abroad, or from public or private research centers.

L'archive ouverte pluridisciplinaire **HAL**, est destinée au dépôt et à la diffusion de documents scientifiques de niveau recherche, publiés ou non, émanant des établissements d'enseignement et de recherche français ou étrangers, des laboratoires publics ou privés.

Two-stage partial melting during the Variscan extensional tectonics

(Montagne Noire, France)

Marc Poujol^{a,*}, Pavel Pitra^a, Jean Van Den Driessche^a, Romain Tartèse^{b,c}, Gilles Ruffet^a, Jean-Louis Paquette^d, Jean-Charles Poilvet^a

^aGéosciences Rennes, UMR CNRS 6118, OSUR, Université Rennes 1, 35042 Rennes CEDEX, France

^bInstitut de Minéralogie, de Physique des Matériaux et de Cosmochimie, Muséum National d'Histoire Naturelle, Sorbonne Universités, CNRS, UMPC & IRD, 75005 Paris, France–France

^cPlanetary and Space Sciences, The Open University, Walton Hall, Milton Keynes, MK7 6AA, United Kingdom

^dUMR CNRS 6524, Laboratoire Magmas et Volcans, Université Blaise Pascal, 63038 Clermont-Ferrand CEDEX, France

* Corresponding author. Tel.: +33-223236208. Email address: marc.poujol@univ-rennes1.fr (M. POUJOL)

ABSTRACT

One of the striking features that characterise the late stages of the Variscan orogeny is the development of gneiss and migmatite domes, as well as extensional Late Carboniferous and Permian sedimentary basins. It remains a matter of debate whether the formation of domes was related to the well documented late orogenic extension or to the contractional tectonics that preceded. Migmatization and magmatism are expected to predate extension if the domes are compression-related regional anticlines, but they must both precede and be contemporaneous with extension if they are extensional core complexes.

In the Montagne Noire area (southern French Massif Central), where migmatization, magmatism and the deformation framework are well documented, the age of the extensional event was unequivocally constrained to 300-290 Ma. Therefore, dating migmatization in this area is a key point for discriminating between the two hypotheses and understanding the Late Palaeozoic evolution of this part of the Variscan belt. For this purpose, a migmatite and an associated anatectic granite from the Montagne Noire dome were dated by LA-ICP-MS (U-

Th/Pb on zircon and monazite) and laser probe ^{40}Ar - ^{39}Ar (K-Ar on muscovite). Although zircon did not record any Variscan age unequivocally related to compression (380-330Ma), two age groups were identified from the monazite crystals. A first event, at ca. 319 Ma (U-Th/Pb on monazite), is interpreted as a first stage of migmatization and as the emplacement age of the granite, respectively. A second event at ca. 298-295 Ma, recorded by monazite (U-Th/Pb) and by the muscovite ^{40}Ar - ^{39}Ar system in the migmatite and in the granite, could be interpreted as a fluid-induced event, probably related to a second melting event identified through the syn-extensional emplacement of the nearby Montalet leucogranite ca. 295 Ma ago. The ages of these two events post-date the Variscan compression and agree with an overall extensional context for the development of the Montagne Noire dome-shaped massif. Comparison of these results with published chemical (EPMA) dating of monazite from the same rocks demonstrates that the type of statistical treatment applied to EPMA data is crucial in order to resolve different monazite age populations.

Keywords: monazite, LA-ICP-MS, U-Th-Pb dating, muscovite, ^{40}Ar - ^{39}Ar dating, Variscan, Montagne Noire

1. Introduction

Until the late 1980s, wrench tectonics was considered to control the late Palaeozoic tectonic evolution of the Variscan orogen (Arthaud and Matte, 1977). It was interpreted as corresponding to an ultimate phase of N-S compression during the Late Carboniferous, and marked the end of the Variscan continental collision. In such compressive context, the commonly coal-bearing continental sedimentary basins that developed during the very late Carboniferous (305 -295 Ma) were interpreted as pull-apart basins or as related to horsetail splay faults at the termination of strike-slip systems faults (e.g. Arthaud and Matte, 1977, Blès

et al. 1989). The development of widespread continental sedimentary basins during the Permian was attributed to a subsequent pervasive N-S extension that occurred throughout the Variscan domain and was considered to result from a plate kinematics re-arrangement without any causal relation with the previous Variscan continental collision (e.g. Arthaud and Matte, 1977, Blès et al. 1989).

More recently, the late Palaeozoic tectonic evolution has been compared to extensional tectonics of both the Tibetan plateau and the North American Cordillera during the Cenozoic (e.g. Ménard and Molnar 1988; Burg et al. 1994). E-W extension, nearly parallel to the belt took place between 330-305 Ma during escape tectonics driven by still active N-S compression forces. It was followed by a NE-SW to N-S extension between 300 Ma and 260 Ma, which started during the waning shortening, and implies a radical change in extension direction induced by the modification of the boundary conditions and the collapse of the entire chain after continental convergence (e.g. Burg et al. 1994). Both episodes of extension are viewed as a consequence of the previous N-S shortening, extension being induced by the collapse of the crust, considerably thickened during the continental collision, after thermal relaxation. In this interpretation, and contrary to older “compressive” interpretations, the late Carboniferous basins are extensional in origin as well as the Permian basins (Becq-Giraudon and Van Den Driessche 1993).

In both interpretations, the pervasive high-temperature low-pressure (HT-LP) metamorphism and magmatism that occurred throughout the Variscan chain during the late Carboniferous resulted from crustal thickening. A striking feature of this period was the development of gneiss and migmatite domes, such as those found in the Montagne Noire and the Velay areas in the southern part of the French Massif Central. However, the two interpretations disagree on the cause of their development. In the compressive scenario these structures are interpreted as regional anticlines that developed in response to the N-S

shortening (Arthaud et al. 1966; Burg and Matte 1978; Matte et al., 1998), whereas they are interpreted as extensional gneiss domes, similar to the Cenozoic metamorphic core complexes of the Basin and Range province, in the extensional scenario (Van Den Driessche and Brun 1989, 1991; Echtler and Malavieille 1990; Brun and Van Den Driessche 1994). In the first case migmatization and magmatism predate extension. The second interpretation requires thermal relaxation and related rheological softening, and change in boundary conditions in order for the crust to collapse. Consequently, migmatization both precedes and is contemporaneous with the onset of extension, especially because extension can enhance partial melting by adiabatic decompression. In the Montagne Noire gneiss dome, the age of the extensional event was unequivocally constrained to ca. 295 Ma by dating a syntectonic leucogranite emplaced within the northward-dipping normal fault that bounds the gneiss dome to the north and controlled the development of Upper Carboniferous – Lower Permian sedimentary basins (Poilvet et al., 2011).

The Montagne Noire gneiss dome is a typical case where geochronology can yield critical constraints on tectonic models, and where the precision obtained on each individual age is crucial. This becomes even more important in a region that underwent a complex polyphased metamorphic/magmatic history possibly characterised by several phases of mineral growth (involving datable minerals such as zircon, monazite and muscovite) in a relatively short period of time. For the purpose of this study, two samples (a migmatite and an associated granite) from the Montagne Noire dome were selected for geochronological investigations (U-Th-Pb on monazite and zircon and K-Ar on muscovite), in order to discriminate between the two contradictory tectonic interpretations.

2. Geological setting

The Montagne Noire gneiss-migmatite massif is located in the southern French Massif Central (Fig. 1). It is composed of a high-grade gneissic core surrounded by mostly low-grade metasediments. The gneissic core is composed of migmatites and augen orthogneisses, with some fine-grained gneissic intercalations that have been interpreted as either metasediments or mylonitic zones (Bogdanoff et al. 1984; Van Den Driessche and Brun 1992, and references therein). Some of these intercalations contain HP/HT mafic and ultramafic metamorphic rocks, suggesting possible major early tectonic contacts (Bogdanoff et al. 1984; Allabouvette and Demange 1993; Demange et al. 1995). The migmatites resulted mostly from partial melting of sediments, but also of felsic augen orthogneisses (e.g. Bogdanoff et al. 1984; Demange, 1982). Weakly deformed to undeformed anatectic granites intrude both the orthogneisses and the migmatites. The gneissic core is surrounded by weakly metamorphosed or unmetamorphosed lower to middle Palaeozoic sediments that are intensely deformed by southward verging folds and thrust faults (e.g. Arthaud 1970; Bogdanoff et al. 1984; Echtler 1990). Late Carboniferous to Early Permian detrital sediments unconformably overlie these tectonic units to the South. In contrast, to the North, the EW-trending north-dipping normal fault zone (Espinouse detachment) marks the tectonic contact between these sediments and the core units, and controls the development of the Lodève-Graissessac and Saint-Affrique basins (Fig. 1; Van Den Driessche and Brun 1989, 1992; Burg et al. 1994).

The foliation of the gneissic core developed within the lower crust during the thrusting event responsible for the deformation of the lower to middle Palaeozoic sedimentary cover. Its dome-shaped structure and tectonic evolution is a matter of debate since long. Three types of models have been proposed ranging from a diapir (e.g. Schuilling 1960; Faure and Cottureau 1988) a double megafold (Arthaud 1970; Burg and Matte 1978; Bogdanoff et al. 1984) or a core complex (Van den Driessche and Brun 1989, Echtler and Malavielle 1990). Many recent models combine in a more or less complex way the processes responsible for these three

types of structures to explain the final structure of the Montagne Noire: diapirism coeval with compression (Faure et al. 2010), compression and subsequent extension (e.g. Cassard et al., 1993; Franke et al. 2011, Doublier et al. 2015, Rabin et al. 2015), compression during extension (Rey et al. 2011), or compression, diapirism and extension (e.g. Soula et al. 2001, Charles et al. 2009). The precise structure of the Montagne Noire dome-shaped massif is beyond the scope of the present paper. We just note that structural and metamorphic analyses have not allowed to reach a consensus, although these different models are built from mostly similar (especially structural) data (e.g. Rey et al. 2011, Van Den Driessche and Pitra 2012). We conclude that until now, discriminating data are lacking to arbitrate between these models.

On the scale of the Variscan belt, the tectonic origin of the Montagne Noire massif is emblematic of the two end-member interpretations discussed before (i.e. compressive or extensive). Eventually, the two main questions are the timing of (1) the development of the HT-LP metamorphism, including partial melting, and (2) the initiation of the extensional tectonics, which predominates during Permian times.

Previous geochronological works on the protolith of the augen orthogneisses yielded Ordovician U-Pb zircon ages (456 ± 3 for Pont-de-Larn, 450 ± 6 Ma for the Gorges d'Héric, Roger et al. 2004, 2015; 455 ± 2 Ma for the Saint-Eutrope gneiss, Pitra et al. 2012). According to Faure et al. (2010), migmatization took place between 333 and 326 Ma (EPMA dating on monazite) while the emplacement of late anatectic granitoids took place between 325 and 316 Ma (including the Vialais granite at 320 ± 3 Ma and Montalet leugranite at ca. 330 Ma, Fig. 1). However, a recent study by Roger et al. (2015) documented an emplacement age of ca 303 Ma (U-Th-Pb on monazite) for the Vialais granite, while the Montalet leucogranite yielded monazite and zircon U-Th-Pb emplacement ages of ca 294 Ma (Poilvet et al. 2011).

Three monazite grains from the Gorges d'Héric orthogneiss yielded $^{206}\text{Pb}/^{238}\text{U}$ ID-TIMS dates around 310 Ma interpreted as a metamorphic age (Roger et al. 2015). Franke et al. (2011) reported a similar age of 313 Ma for monazite extracted from a foliated aplite dyke from the Gorges d'Héric, while Maluski et al. (1991) reported a biotite K-Ar plateau age of 316 ± 4 Ma for the Caroux massif. The undeformed garnet-bearing leucogranite of Ourtigas yielded a U-Th-Pb age of ca 298 Ma (Roger et al. 2015). Finally, a monazite Th-Pb age of 294.4 ± 4 Ma (Pitra et al. 2012) as well as ^{40}Ar - ^{39}Ar ages on muscovite and biotite of ca. 297 Ma (Maluski et al. 1991) have been obtained for orthogneiss samples sheared along the Espinouse detachment.

3. Sampling and petrography

Two samples were selected for this study (Fig. 1): 1) a cordierite-bearing granite located in the central part of the dome (sample ES7), and a migmatite (sample ES8), spatially associated with the cordierite-bearing granite. Both rocks were sampled at the same locations as their equivalent dated by Faure et al. (2010). One of the main reasons for this sampling strategy is linked to the fact that previous dating (EPMA on monazite) by Faure et al. (2010) on the Montalet granite returned an age (327 ± 7 Ma) that is very different from the age (294 ± 1 Ma; U-Th-Pb on monazite) obtained by Poilvet et al. (2011) on the same granite. This age difference was also noticed by Roger et al. (2015) for the Vialais granite. Therefore, the age discrepancies cast some doubts on the EPMA ages obtained by Faure et al. (2010) on the Laouzas cordierite-bearing granite and the spatially associated migmatite. They have also been chosen because of the potentially complex history that these rocks underwent between 340 and 290 Ma.

3.1 Laouzas granite, sample ES7

The Laouzas granite (Fig. 1) crops out in the west-central part of the axial zone of the Montagne Noire dome. It was sampled near the Laouzas dam (43°38'7.35"N, 2°45'10.00"E). The rock is an undeformed heterogeneous coarse-grained (1-5 mm in average, locally up to 3 cm) biotite-bearing granite containing numerous large clusters of cordierite (up to 5 cm), biotite-rich schlieren, tourmaline nodules and dark, foliated mica-rich enclaves (Fig. 2a). Although the schlieren and enclaves locally display a preferred orientation, no solid-state deformation is observed at the grain-scale in the granite, with the exception of a weak undulose extinction of quartz crystals.

The sample is dominated by plagioclase, K-feldspar and quartz, and contains subordinate amounts of biotite, cordierite and muscovite (Fig. 2b). Dumortierite, tourmaline, andalusite and sillimanite are present locally. Plagioclase forms euhedral to subhedral stubby prismatic crystals, 1-3 mm long. Plagioclase cores are generally altered (saussuritised) and surrounded by a clear rim (Fig. 2c). The rims are similar to feldspar that also fills fractures in the plagioclase cores. Some plagioclase rims are intergrown with tiny crystals of quartz in a granophyric, myrmekite-like texture, in particular at the contact with K-feldspar. K-feldspar and quartz are anhedral, 1-5 mm in size. Cordierite forms anhedral crystals (up to 2 mm) that are slightly pinitised or replaced by fine-grained muscovite around the rims (Fig. 2b). Biotite crystals (0.1-3 mm) are subhedral and locally partly altered to chlorite in association with needles of rutile (sagenite). Rare minute needles of sillimanite are locally present in large quartz crystals. Although euhedral muscovite crystals (~1 mm) are locally present, muscovite mostly forms large subhedral poikiloblasts (up to 2 mm) or develops tiny crystals at the expense of K-feldspar, plagioclase or cordierite. Needles of dumortierite (pink to violet, strongly pleochroic acicular crystals, ~0.5 mm) or tourmaline (pale green, ~0.3 mm) are

commonly associated with clear plagioclase overgrowths, anhedral pink andalusite (~0.5 mm) and muscovite (Fig. 2c).

These observations suggest a two-stage evolution. The crystallisation of the relatively coarse-grained granite (plagioclase cores, K-feldspar, quartz, biotite, cordierite, \pm muscovite \pm sillimanite) was followed by a second event resulting in the crystallisation of the plagioclase rims, dumortierite, tourmaline, andalusite and muscovite. The second stage was possibly associated with the alteration of the plagioclase cores and biotite. It could be either magmatic or, more probably, hydrothermal in origin. The hydrothermal origin is supported by the textures and in particular the position of the boron-bearing minerals. Indeed, tourmaline and dumortierite are known to be related to hydrothermal alteration (e.g. Taner and Martin, 1993), but are liquidus rather than late-stage phases in leucogranitic magmatic systems (Benard et al., 1985).

3.2 La Salvetat migmatite, sample ES8

The La Salvetat migmatite crops out in the central part of the axial zone of the Montagne Noire gneiss dome, generally to the south of the Laouzas granite (Fig. 1). It was sampled ca. 2 km south of the Laouzas dam, close to the summit of a hill called Al Rec del Bosc (43°37'1.65"N, 2°45'23.70"E). The rock is a banded stromatic migmatite (Fig. 2d) and is locally garnet-bearing. The foliation is defined by a weak preferred orientation of biotite that is parallel to alternating layers of leucosome, mesosome and biotite-dominated melanosome. Leucosomes are relatively coarse-grained (0.5-3 mm), up to 1 cm thick, and are composed of subhedral plagioclase, quartz and subordinate K-feldspar, and locally contain cordierite, muscovite, biotite and tourmaline (Fig. 2e). Tourmaline commonly forms anhedral to subhedral interstitial, optically zoned grains. Plagioclase and K-feldspar have a dusty

appearance and plagioclase is partly replaced by zoisite/clinozoisite and white mica (Fig. 2f). Cordierite is subhedral and partly altered to pinite. Biotite is locally partly replaced by chlorite and contains lenses of minute prehnite (?) or clay minerals that are parallel to the (001) cleavage (Fig. 2f), in particular in the leucosome and in the adjacent melanosome. Euhedral muscovite is locally present in the leucosome. Subhedral muscovite, forming either fine-grained clusters or larger poikilitic crystals, commonly develops at the expense of biotite, cordierite and feldspars in the leucosomes.

These observations suggest at least two stages of evolution, where the migmatite textures, attributable to partial melting, are partly overprinted by hydrothermal alteration. The geographic proximity and the common petrographic character of the leucosomes and the Laouzas granite suggest a genetic relation between the two. Therefore, the La Salvetat migmatite is interpreted to be a likely source for the anatectic Laouzas granite.

4. U-Th-Pb LA-ICP-MS and ^{40}Ar - ^{39}Ar dating

4.1 Analytical techniques

4.1.1 NanoSIMS analytical protocol

The distribution of selected species was imaged in some monazite grains using the NanoSIMS 50 ion probe at the University of Rennes 1. Secondary ion images of ^{89}Y , ^{139}La , ^{140}Ce , ^{149}Sm , ^{206}Pb , ^{208}Pb , ^{232}Th and $^{238}\text{U}^{16}\text{O}$ were collected using the same primary O- beam of ~ 170 pA over $90\text{ }\mu\text{m} \times 90\text{ }\mu\text{m}$ areas. The mass resolving power was set to ~ 3500 , sufficient to readily resolve isobaric interferences such as $^{143,145}\text{NdPO}_2$ on $^{206,208}\text{Pb}$. A single plane of image data, divided in $128\text{ px} \times 128\text{ pixels}$, was collected using a dwell time of 40 ms/pixel, representing an acquisition time of ~ 11 min for each area. The raw image data were processed using the

251 L'image (Larry Nittler, Carnegie Institute of Washington, USA;
252 http://home.dtm.ciw.edu/users/nittler/limage/limage_manual.pdf) and ImageJ softwares.

253

254 4.1.2 U-Th-Pb dating technique

255 A classic mineral separation procedure has been applied to concentrate minerals suitable for
256 U-Th-Pb dating using the facilities available at Géosciences Rennes (see Poilvet et al., 2011).
257 Zircon and monazite grains were carefully handpicked under a binocular microscope and
258 embedded in epoxy mounts. The grains were then polished on a lap wheel with a 6 µm and 1
259 µm diamond suspension successively. Zircon grains were imaged by cathodoluminescence
260 (CL) using a Reliotron CL system equipped with a digital colour camera available in
261 Géosciences Rennes and monazite grains by backscattered electron imaging on a JEOL JSM
262 6400 as well as by NanoSIMS. In addition, monazite grains have also been identified in thin
263 sections in order to date them in context.

264 U-Th-Pb geochronology of zircon and monazite was conducted by *in situ* laser
265 ablation inductively coupled plasma mass spectrometry (LA-ICP-MS) at the Laboratoire
266 Magmas et Volcans in Clermont-Ferrand, France. Ablation spot diameters of 26 µm and 7 µm
267 with repetition rates of 3 Hz and 1 Hz were used for zircon and monazite, respectively. Data
268 were corrected for U-Pb and Th-Pb fractionation and for the mass bias by standard
269 bracketing with repeated measurements of the 91500 zircon (Wiedenbeck et al. 1995) or the
270 Moacyr monazite standards (Gasquet et al. 2010). Repeated analyses of GJ-1 zircon (607 ± 15
271 Ma, N=6; Jackson et al. 2004) or Manangoutry monazite (554 ± 23 Ma, N=6; Paquette and
272 Tiepolo 2007) standards treated as unknowns were used to control the reproducibility and
273 accuracy of the corrections. Data reduction was carried out with the GLITTER® software
274 package developed by the Macquarie Research Ltd. (Jackson et al. 2004). Concordia ages and
275 diagrams were generated using Isoplot/Ex (Ludwig 2001). All errors given in Table 1 and 2

are listed at one sigma, but where data are combined for regression analysis or to calculate weighted means, the final results are provided with 95% confidence limits. Further information on the instrumentation and the analytical technique is detailed in Hurai et al. (2010).

For each grain analyzed (zircon and monazite) we also estimated the concentrations of U, Th and Pb as follows. First, the drift factor was calculated using the parameter a and b of a linear regression of the average ^{206}Pb counts per second (cps) for all the standards measured during the course of the analyses as a function of their position during the acquisition.

$$(1) \text{}^{206}\text{Pb}_{\text{cps}} = a \times N + b$$

with $\text{}^{206}\text{Pb}_{\text{cps}}$ = average measured values for the standard in cps corrected from the blank, a = slope of the regression, b = ordinate at origin and N = analysis number.

The drift factor for each analysis (DF^N) is then calculated as follows:

$$(2) DF^N = \frac{b}{(a \times N + b)}$$

Then the Pb, Th and U concentrations are calculated using the known concentrations of these elements in the standards following:

$$(3) C_{\text{sample}}^N_{\text{ppm}} = C_{\text{sample}}^N_{\text{meas}} \times DF^N \times \frac{C_{\text{std}}_{\text{real}}}{C_{\text{std}}_{\text{aver}}}$$

with N = analysis number, $C_{\text{sample}}^N_{\text{ppm}}$ = calculated concentration of the element in ppm,

$C_{\text{sample}}^N_{\text{meas}}$ = measured values of the element in cps, DF^N = drift factor calculated for this analysis, $C_{\text{std}}_{\text{real}}$ = known concentration of the standard and $C_{\text{std}}_{\text{aver}}$ = drift-corrected average value for all the standards measured during the course of the analyses.

4.1.3 Ar-Ar dating technique

Single grains of muscovite used for the experiments were handpicked under a binocular microscope from 0.25–1.00 mm fractions of crushed rock samples. Care was taken to select

inclusion-free crystals of about 1 mm in size, in order to avoid large poikilitic crystals as well as fine-grained clusters.

The samples were wrapped in Al foil to form small packets (11 × 11 mm) that were stacked up to form a pile within which packets of fluence monitors were inserted every 10 samples. Irradiation was performed at the HFR Petten reactor (Petten, the Netherlands) in the Cd-shielded Rodeo P3 facility and lasted 72h ($J/h \approx 2.54 \times 10^{-4} \text{ h}^{-1}$). The irradiation standard was amphibole Hb3gr (Turner et al. 1971; Roddick 1983, Jourdan et al. 2006; Jourdan and Renne 2007), with an age of $1081.0 \pm 1.2 \text{ Ma}$ (Renne et al. 2010, 2011).

Step-heating analyses of single grains were performed with a CO₂ laser probe coupled to a Map215® mass spectrometer. The experimental procedure is described in Ruffet et al. (1991) and Ruffet et al. (1995). The five argon isotopes and the background baselines were measured in eleven cycles, in peak-jumping mode. Blanks were performed routinely each first or third/fourth run, and subtracted from the subsequent sample gas fractions. All isotopic measurements are corrected for K, Ca and Cl isotopic interferences, mass discrimination and atmospheric argon contamination. Apparent age errors are plotted at the 1σ level and do not include the errors on the $^{40}\text{Ar}^*/^{39}\text{Ar}_K$ ratio and age of the monitor and decay constant. The errors on the $^{40}\text{Ar}^*/^{39}\text{Ar}_K$ ratio and age of the monitor and decay constant are included in the final calculation of the (pseudo-)plateau age error margins or for apparent ages individually cited. Details on the method and $^{40}\text{Ar}/^{39}\text{Ar}$ analytical data are given in the Supporting Information.

It is commonly considered that a plateau is obtained when calculated $^{40}\text{Ar}^*/^{39}\text{Ar}_K$ ratios of at least three consecutive steps, containing a minimum of 70% of the ^{39}Ar released, agree with the weighted mean calculated $^{40}\text{Ar}^*/^{39}\text{Ar}_K$ ratio of the plateau segment. Pseudo-plateau ages can be defined with less than 70% of the ^{39}Ar released. All ages are displayed at the 1σ level. Analytical data, parameters used for calculations (isotopic ratios measured on K,

Ca and Cl pure salts; mass discrimination; atmospheric argon ratios; J parameter; decay constants...) and reference sources are available in a complementary data repository.

4.2 U-Th-Pb LA-ICP-MS and ^{40}Ar - ^{39}Ar results

4.2.1 Sample ES7 – Laouzas granite

Zircon and monazite grains were both recovered from this sample. Most of the zircon grains were pink in colour, euhedral, with very variable shapes from elongated to oval. Cathodoluminescence imaging revealed a rather heterogeneous population with anything from homogeneous low luminescent to heterogeneous (core + rim) grains (Fig. 3A). Thirty-seven analyses out of twenty-six zircon grains were made (Table 1). The heterogeneity of the grains is confirmed in a Tera-Wasserburg diagram (Fig. 4A) where data points plot in a concordant to very discordant position with apparent $^{207}\text{Pb}/^{206}\text{Pb}$ ages ranging from 1010 Ma down to 370 Ma. Because of this heterogeneity, which is probably caused by a complex mixing of heterogeneous inheritance, plus variable degree of common Pb content and Pb loss, it is not possible to calculate any relevant ages. We therefore favoured plotting the data in a relative probability plot diagram (Fig. 4E) where only the $^{207}\text{Pb}/^{206}\text{Pb}$ apparent ages for the more than 90% concordant points were considered. One main peak can be defined at ca. 500 Ma, with minor peaks around 700 and 800 Ma.

Two types of monazite grains were found in this sample. Type 1 monazite comprises euhedral dark brown grains with sharp concentric zoning (Fig. 5) and type 2 monazite comprises euhedral to subhedral yellowish to orange grains characterised by complex patchy zoning (Fig. 6), as revealed by backscattered electron (BSE) imaging. Elemental imaging carried out using the NanoSIMS ion probe reveals that the concentric zoning for type 1 monazite (Fig. 5) is visible with all the elements imaged (Y, La, Ce, Sm, U, Th and Pb) with cores that are LREE-rich and poor in Y, U, Th and Pb. More importantly, the distributions of

U and Th in this monazite type perfectly match each other. For type 2 monazite (Fig. 6), the complex zoning noticed in BSE images is well mimicked by the distribution of Y, REE, U and ^{206}Pb while the distribution of Th and ^{208}Pb is less disturbed.

These two types of monazite grains were therefore analyzed separately. In addition, 19 analyses (11 grains) were performed directly in a thin section. In total, 50 analyses were carried out (Table 2). Plotted in a $^{206}\text{Pb}/^{238}\text{U}$ versus $^{208}\text{Pb}/^{232}\text{Th}$ concordia diagram (Fig. 4B), the two types plot in two distinct groups. For the monazite grains dated in context in the thin sections, there is no evident correlation between the mineral hosting the monazite grains and their apparent ages. Therefore, the location of type 1 and type 2 monazite is not related to any specific host mineral. Type 1 monazite (N = 26; grains with sharp concentric zoning) plots in a concordant to slightly discordant position. A cluster of 14 concordant analyses (Fig. 4B) yields a concordia age (Ludwig 1998) of 318.0 ± 1.4 Ma (MSWD=0.87). This concordia age is equivalent within error to the average $^{206}\text{Pb}/^{238}\text{U}$ date of 318.8 ± 1.5 Ma (N = 26; MSWD = 0.95) obtained for the 26 analyses defining this first group. Interestingly, the $^{208}\text{Pb}/^{232}\text{Th}$ apparent ages for this group display a bimodal distribution (see Fig. 4G), with one peak at 331.5 ± 2 Ma and a second one at 319.1 ± 2.0 Ma.

Data obtained on type 2 monazite (grains with complex patchy zoning; N = 20) exhibits a slight reverse discordance (Fig. 4B). The mean $^{206}\text{Pb}/^{238}\text{U}$ date obtained for these twenty analyses is consistent with a value of 293.5 ± 1.7 Ma (MSWD = 0.78) while the $^{208}\text{Pb}/^{232}\text{Th}$ apparent dates yield average dates of 285.2 ± 2.2 Ma (MSWD = 0.66; N = 8) for the grains analysed in the epoxy puck and of 296.5 ± 2.8 Ma (MSWD = 0.42; N = 7) for the grains dated in the thin section (Fig. 4G).

Muscovite single grain from sample ES7 yielded a flat ^{40}Ar - ^{39}Ar age spectrum (Fig. 4H) over most of $^{39}\text{Ar}_K$ degassing (ca. 95%), corresponding to a calculated plateau age of 298.2 ± 0.8 Ma (2σ level).

4.2.2 Sample ES8 – La Salvetat migmatite

Both monazite and zircon grains were extracted from this sample. Two types of zircon grains were found. The first type is characterized by elongate pinkish grains (Fig. 3B), while the second type is constituted by squat prismatic grains (Fig. 3C). Both types display complex zoning with core and rims apparent for most (Fig. 3B and C). Thirty-two analyses were performed on twenty-eight grains (Table 1). Plotted in a Tera-Wasserburg diagram (Fig. 4C), they plot in a concordant to discordant position, with apparent $^{207}\text{Pb}/^{206}\text{Pb}$ ages ranging from ca. 2650 down to 300 Ma. Once again, it is difficult to get any valuable geochronological constraint with this set of data. Plotted in a relative probability plot (Fig. 4E), two main peaks arise at ca. 610 Ma and 875 Ma, with minor peaks at 690, 1000, 1310 and 2450 Ma.

From a morphological point of view, all monazite crystals were yellow and euhedral to subhedral. Forty-six analyses were performed (38 on separated grains and 8 directly in context in thin sections). Plotted in a $^{206}\text{Pb}/^{238}\text{U}$ versus $^{208}\text{Pb}/^{232}\text{Th}$ concordia diagram (Fig. 4D), they all plot in a concordant to slightly discordant position. A first group of 14 analyses defines a concordia ages of 318.5 ± 0.7 Ma (MSWD = 1.3; Fig. 4D). A second cluster of 15 analyses yields a concordia age of 298.8 ± 1.3 Ma (MSWD = 0.68; Fig. 4D). The remaining 17 analyses plot in a slightly reverse discordant position either between the two previous calculated concordia dates or are apparently younger than 299 Ma (Fig. 4D). The two analyses performed in monazite grains hosted by quartz yielded dates close to 290 Ma while the monazite grains hosted by biotite plot in a scattered position.

When looking at the BSE imaging, the first group (ca. 318.5 Ma) is characterized by fairly homogeneous monazite grains (Fig. 7), while monazite in the second group (ca. 299 Ma) is characterized by more patchy zoning (Fig. 8). The NanoSIMS imaging of the first group confirms the rather homogeneous distribution of the imaged elements with the

exception of U and ^{206}Pb that appear to be poorer in the core of the grain (Fig. 7). For the second group, the elemental distributions are not as simple. The REE distribution seems to be homogeneous throughout the grain whereas the Y, U, Th and Pb distributions are patchier (Fig. 8).

Similar to monazite in ES7, monazite data in ES8 are characterized by evident differences between the $^{206}\text{Pb}/^{238}\text{U}$ and the $^{208}\text{Pb}/^{232}\text{Th}$ dates (Fig. 4F and G). The $^{208}\text{Pb}/^{232}\text{Th}$ dates fall into 3 distinct populations (Fig. 4G) at 319.8 ± 1.8 Ma (MSWD = 1.3; N = 15), 298.2 ± 1.5 Ma (MSWD = 0.89; N = 19) and 284.7 ± 2.1 Ma (MSWD = 0.98; N = 8), respectively. $^{206}\text{Pb}/^{238}\text{U}$ dates define two different peaks at 316.2 ± 1.9 Ma (MSWD = 0.68; N = 15) and 296.1 ± 1.3 Ma (MSWD = 2.8; N=26), respectively (Fig. 4F).

Muscovite single grain from sample ES8 yielded a flat ^{40}Ar - ^{39}Ar age spectrum (Fig. 4H) over most of ^{39}ArK degassing (ca. 98%) that correspond to a calculated plateau age of 298 ± 1 Ma (2σ level). This age is similar to the ES7 plateau age.

5. Geological significance of the geochronological data

5.1 Zircon dating

Zircon data from both the Laouzas granite and the La Salvetat migmatite show a considerable spread (Fig. 4E) and cannot be used to either date the emplacement of the granite or the age of migmatization. They rather demonstrate the existence of a complex polygenic history in the region, with dates ranging from the late Archean to the Ordovician. They are consistent with the data published by Faure et al. (2010), although more date populations were found in our study. In the La Salvetat migmatite, the youngest point (grain 1.1d) that plots close to the concordia gives a $^{207}\text{Pb}/^{206}\text{Pb}$ date of 337 ± 27 Ma (1 sigma). This grain might have grown

during the migmatization, but because of its large error, it does not help to constrain this event precisely.

5.2 Monazite dating

5.2.1 The Laouzas granite

In the $^{206}\text{Pb}/^{238}\text{U}$ versus $^{208}\text{Pb}/^{232}\text{Th}$ concordia diagram (Fig. 4B), the monazite grains from the Laouzas granite plot in two clusters although the geochronological information brought, for each cluster, by the monazite grains $^{206}\text{Pb}/^{238}\text{U}$ and $^{208}\text{Pb}/^{232}\text{Th}$ respective dates is different. Indeed, within each cluster, the $^{206}\text{Pb}/^{238}\text{U}$ dates are comparable, while they are more scattered in the case of the $^{208}\text{Pb}/^{232}\text{Th}$ ones.

To first order, four dates can be defined for the Laouzas granite. The oldest date at ca. 330 Ma can be calculated using the older apparent $^{208}\text{Pb}/^{232}\text{Th}$ dates (Fig. 4G). The second one around 319 Ma is given by a concordia age of 318.0 ± 1.4 Ma (Fig. 4B), the mean $^{206}\text{Pb}/^{238}\text{U}$ date of 318.8 ± 1.5 Ma obtained for all the analyses from the older cluster (Fig. 4B) and from one of the peaks defined by the $^{208}\text{Pb}/^{232}\text{Th}$ dates at 319.1 ± 2.0 Ma (Fig. 4G). The third date of around 298-292 Ma is defined by one peak in the $^{208}\text{Pb}/^{232}\text{Th}$ dates distribution at 298.2 ± 1.5 Ma (Fig. 4G) and the mean $^{206}\text{Pb}/^{238}\text{U}$ date of 293.5 ± 1.7 Ma calculated for the second group (Fig. 4B). This third date is in a good agreement with the ^{40}Ar - ^{39}Ar age of 298.2 ± 0.8 Ma (2σ level) obtained on muscovite from the same sample (Fig. 4H). Finally, the youngest date around 285 Ma is defined by the youngest $^{208}\text{Pb}/^{232}\text{Th}$ dates (Fig. 4G).

It seems evident that the dates of ca. 319 Ma and ca. 298 Ma are representative of specific events as they are common to both chronometers (U/Pb and Th/Pb) and because the second one is also defined by ^{40}Ar - ^{39}Ar dating. Therefore, two scenarios can be suggested. Either the date of ca. 319 Ma yields the emplacement age of the Laouzas granite and the date of ca. 298 Ma is related to a post emplacement event, or the granite was emplaced ca. 298 Ma ago, in which case the date of ca. 319 Ma should be regarded as “inherited”. Three

observations are helpful to discriminate between these two scenarios. (i) The backscattered imaging shows that the ca. 319 Ma monazite population (Type 1) is characterized by a rather simple concentric zoning, whereas the ca. 298 Ma old population (Type 2) systematically displays a complex patchy zoning. Concentric zoning is consistent with a magmatic origin, whereas patchy zoning suggests the involvement of a post-crystallization perturbing event, such as fluid-related dissolution/recrystallization (Williams et al. 2011; Tartèse et al. 2011; Didier et al. 2013). (ii) As noticed on the NanoSIMS imaging (Fig. 5 and 6), the elemental distributions perfectly match for the Type 1 monazite while they differ for Type 2. (iii) Finally, petrographic observations suggest an overprint of the primary magmatic assemblage associated with a later circulation of hydrothermal fluids. In the light of these observations, we propose that the Laouzas granite was emplaced ca. 319 Ma ago and was affected by a post-emplacement, fluid-related event, ca. 298 Ma ago. In this case, the ^{40}Ar - ^{39}Ar age at 298.2 ± 0.8 Ma yielded by muscovite from the same sample would also characterize this late hydrothermal event, since it has been shown that the K-Ar geochronometer in muscovite can be highly sensitive to fluid circulations in granites in a similar context (Questembert leucogranite, Armorican massif, France) by Tartèse et al. (2011).

The oldest date at ca. 330 Ma is only evidenced by the $^{208}\text{Pb}/^{232}\text{Th}$ dates. A similar phenomenon has also been noticed by Tartèse et al. (2012) for monazite grains from a mylonitized granite from the South Armorican Shear Zone, in which the $^{208}\text{Pb}/^{232}\text{Th}$ dates (defining an average date of 313 ± 3 Ma) were systematically older than the U-Pb dates (defining an average date of 299 ± 4 Ma). A recent study by Didier et al. (2013) has demonstrated that F-rich fluids can be responsible for the disturbance of the Th/Pb ratios in monazite and the incorporation of excess Pb, leading to a large spread of the $^{208}\text{Pb}/^{232}\text{Th}$ dates. Disturbed $^{208}\text{Pb}/^{232}\text{Th}$ and $^{206}\text{Pb}/^{238}\text{U}$ data were also obtained by Poitrasson et al. (2000) and were attributed to variable inputs and/or depletions in U, Th and Pb in the monazite

crystals during hydrothermal alteration. As detailed earlier, the Laouzas anatectic granite bears petrographic evidence of hydrothermal fluid circulation. We therefore believe that this date of ca. 330 Ma is meaningless and is attributed to fluid perturbation of some of the monazite grains leading to a fractionation of their Th/Pb ratios (cf. Didier et al. 2013).

The other date at ca. 285 Ma is also obtained with only the $^{208}\text{Pb}/^{232}\text{Th}$ dates. Once again, either this date is related to a fluid-induced perturbation of the monazite Th-Pb isotope system, and is, therefore, meaningless, or it reflects the age of a yet unknown event in the region.

5.2.2 La Salvetat migmatite

Monazite from the La Salvetat migmatite also yields different $^{208}\text{Pb}/^{232}\text{Th}$ and $^{206}\text{Pb}/^{238}\text{U}$ dates but here again two main dates can be proposed. A first one at ca. 319 Ma is given by a concordia age of 318.5 ± 0.7 Ma (Fig. 4D), a mean $^{208}\text{Pb}/^{232}\text{Th}$ date of 319.8 ± 1.8 Ma (Fig. 4G) and a mean $^{206}\text{Pb}/^{238}\text{U}$ date of 316.2 ± 1.9 Ma (Fig. 4F). The second one, around 298 Ma, is given by a concordia age of 298.8 ± 1.3 Ma (Fig. 4D), a mean $^{208}\text{Pb}/^{232}\text{Th}$ date of 298.2 ± 1.5 Ma (Fig. 4G), a mean $^{206}\text{Pb}/^{238}\text{U}$ date of 296.1 ± 1.3 Ma (Fig. 4F) and a muscovite ^{40}Ar - ^{39}Ar plateau age of 298 ± 1 Ma (Fig. 4H).

Lastly, the youngest $^{208}\text{Pb}/^{232}\text{Th}$ dates define a mean date of 284.7 ± 2.1 Ma. Monazite is known to be very resistant to diffusional reequilibration (e.g. Seydoux-Guillaume et al. 2002; Gardés et al. 2007), preserving the age of their crystallisation. On the other hand, they recrystallize readily by dissolution/precipitation processes, when fluids or magmas are involved (Williams et al. 2011; Tartèse et al. 2011; Didier et al. 2013). As a general rule, two major “pulses” of monazite growth are predicted in metapelitic rocks: subsolidus growth in the upper amphibolite facies and growth during the cooling of leucosomes (rather than partial melting) following migmatization (e.g. Foster et al. 2000; Rubatto et al. 2001; Kelsey et al. 2008; Spear and Pyle 2010). Furthermore, it is now well established that monazite may

(re)crystallise due to fluid-rock interactions relatively late in the metamorphic history (e.g. Bosse et al. 2009; Tartèse et al. 2011, 2012; Didier et al. 2013).

Consequently, the three dates of ca. 319, ca. 298 and ca. 284 Ma obtained for the monazite grains from the La Salvetat migmatite, may represent the ages of: (1) crystallisation during the prograde metamorphism in the upper amphibolite facies conditions; (2) crystallisation of the leucosomes following partial melting and (3) recrystallisation due to late fluid circulations, respectively. On the other hand, the close spatial and inferred genetic association of the migmatites with the Laouzas granite suggests that monazite grains of the same age should be found in both rock types. The crystallisation of the Laouzas granite is inferred to have taken place at ca. 319 Ma (see earlier), suggesting that the date of 319 Ma in the La Salvetat migmatite should be interpreted as the age of the crystallisation of the leucosomes, rather than that of the prograde amphibolite-facies metamorphism. The second date of ca. 298 Ma found in the migmatite is identical within error to the date of ca. 298 Ma found in the Laouzas granite, but also to the emplacement age of 294 ± 3 Ma (U-Pb on zircon) obtained for the syntectonic Montalet leucogranite (Poilvet et al. 2011), situated about 20 km to the NW (Fig. 1). It is conceivable that a second phase of partial melting of the La Salvetat migmatite was the source of this leucogranite but the poor outcrop conditions do not allow to validate such hypothesis. Alternatively and more probably, partial melting of other deeper formations formed the Montalet magmas, which percolated with associated fluids through the crust, resulting in the recrystallization of some monazite grains in the migmatite-granite dome, as suggested by the late fluid circulations inferred from the petrographic observations of the La Salvetat migmatite. A detailed study of the geochemical affinities between the migmatites and the various granites would be necessary to answer this question.

Finally, the 284 Ma date, identical within uncertainty to the date of ca. 285 Ma obtained in the Laouzas granite is, as argued above, either an artefact due to fluid-enhanced

modification of some of the monazite crystals, or, an evidence of a younger, although unidentified, event in the region. Similar Permian ages are known elsewhere in the European Variscan belt. Mougeot et al. (1997) reported an U-Pb apatite age ca. 289 Ma for the Velay granite. Cathelineau et al. (1990) obtained Permian ages on vein-type deposits from the Mortagne district in the South Armorican Massif and the French Massif Central, with a major stage of uranium mobilization between 290 and 260 Ma. In the Erzgebirge (Germany), the emplacement of vein-type deposits is also Permian in age and postdates the emplacement of the youngest Variscan granites by no less than 20-25 Ma (e.g. Velichkin and Vlasov, 2011 and references therein). More recently, Boutin et al. (2015) reported some Permian U-Pb ages obtained on titanite associated with chlorite-talc mineralization in the Pyrenees. This non-exhaustive list demonstrates that this date of ca. 285 Ma is not unique at the scale of the Variscan belt as numerous ore deposits linked to fluid circulations are contemporaneous, and could, therefore, be considered as meaningful for the Montagne Noire. Finally, the remaining data that plot in a scattered position (Fig. 4D) could be attributed to an incomplete resetting of their U-Th-Pb system during the subsequent fluid circulation events.

5.3 Partial melting and regional correlations

In summary, the Laouzas granite and the La Salvetat migmatite are spatially close and petrographically similar. The Laouzas granite is therefore interpreted as a product of the partial melting recorded in the La Salvetat migmatite. Monazite grains from both rocks recorded a date of ca. 319 Ma, which is interpreted as the emplacement age of the Laouzas granite, and hence also that of a first stage of migmatization (or rather the crystallisation of the leucosomes resulting from this partial melting). The date of ca. 298 Ma is tentatively attributed either to a second stage of migmatization, or more probably to a pervasive percolation of magmas and associated fluids coming from a deeper source and resulting in the syntectonic crystallisation of the more superficial Montalet leucogranite.

It is interesting to draw a parallel with the scenario described for the Velay gneiss dome, located some 150 km ENE of the Montagne Noire. In this area, Montel et al. (1992) described two successive stages of migmatization that have been dated at 314 ± 5 Ma and 301 ± 5 Ma (U-Pb ID-TIMS on monazite, Mougeot et al., 1997). Barbey et al. (2015) suggest three melting events, estimated to have occurred at 325-315 Ma, ca. 305 Ma, and 305-295 Ma. In addition, Roger et al. (2015) bracketed the high temperature deformation and metamorphism both in the Gorges d'Héric and the Vialais granite between 310-300 Ma.

6. Tectonic implications for the formation of the Montagne Noire dome

Two major hypotheses are proposed at present to explain the origin of the Montagne Noire dome. Both agree on the presence of compressional and extensional features, but disagree on their timing and their relative importance. The first hypothesis considers that the domal structure developed as a regional anticline during the collisional stage of the Variscan orogeny (e.g. Arthaud et al. 1966; Burg and Matte 1978, Charles et al. 2009) and interpret the extensional features as second-order and late with respect to the formation of the dome. For the second hypothesis, dome-like exhumation of the lower continental crust beneath a major crustal-scale extensional detachment is at the origin of the Montagne Noire dome (Van Den Driessche and Brun 1989; Echtler and Malavieille 1990; Van Den Driessche and Brun 1992). Beyond the structural record, this second hypothesis is supported and constrained in time by the syntectonic emplacement of a leucogranite at ca. 295 Ma (Poilvet et al. 2011) and by monazite and mica ages of ca. 295 Ma in sheared metasediments and orthogneisses (Maluski et al. 1991; Pitra et al. 2012) along the detachment that is contemporaneous with and controls the development of the Stephanian to Permian Graissessac and Lodève basins (Fig. 1; Van Den Driessche and Brun 1989; Bruguier et al. 2003). In contrast, the advocates of the compressional origin of the dome either associate the extensional structures exclusively with

the compressional phase (Brunel and Languet 1997), or relegate it to a secondary role in the brittle domain (Matte et al. 1998; Charles et al. 2009). The principal argument was the age of the late- to post-kinematic Vialais granite, supposedly dated at 327 ± 5 Ma (TIMS on zircon and monazite fractions; Matte et al. 1998), emplaced in the central-eastern part of the dome (Fig. 1), and the ca. 330 Ma dates obtained by electron probe micro-analysis (EPMA) monazite dating from migmatites and anatectic granites summarised in Charles et al. (2009) and Faure et al. (2010).

In the “compressional” interpretation, migmatization and magmatism predate extension. In the “extensional” interpretation, which requires thermal relaxation and related rheological softening in order for the crust to collapse, migmatization is also contemporaneous with the onset of extension, especially because extension can enhance partial melting by adiabatic decompression (e.g. Hollister 1993; Holtz and Johannes 1994; Holtz et al. 2001; Thompson 2001). Clearly, the clue is to be sought in the absolute timing of regional migmatization and related granite emplacement.

First, the Vialais granite and an associated post-kinematic leucogranite have been recently re-dated at 303 ± 4 Ma and 298 ± 2 Ma, respectively (U-Pb monazite ICP-MS ages, Roger et al. 2015). Second, our data support a genetic link between the migmatites and granites in the “axial zone” of the Montagne Noire gneiss dome. Three age groups were identified from the monazite U-Th/Pb data. A first event, at ca. 319 Ma, is recorded in both the La Salvetat migmatite and the Laouzas granite, and is interpreted as the end of a first stage of migmatization and as the emplacement age of the Laouzas granite, respectively. A second event, at ca. 298 Ma, is recorded in the migmatite and in the Laouzas granite, and could be interpreted as a fluid-induced event, probably related to a second melting event identified through the emplacement of the Montalet and Vialais leucogranites. The third event, dated around 285 Ma, although not clear, could be linked to Permian fluid circulations. The

presence of two stages of partial melting at ca. 320 Ma and ca. 300 Ma confirms (i) the interpretation of the Late Carboniferous-Early Permian evolution of the Variscan belt dominated by the extensional collapse, which predicts migmatization both preceding and contemporaneous of the onset of extension, and (ii) the interpretation of the Montagne Noire dome as an extensional gneiss dome.

7. EPMA versus LA-ICP-MS dating

In recent years, some studies comparing monazite ages obtained by the LA-ICP-MS and EPMA techniques encountered discrepancies between both sets of ages (Paquette and Tiepolo 2007; Poilvet et al. 2011 and references therein). Other studies also pointed out that EPMA dating should be acquired with caution as, for example, incorrect determination of background intensities could result in artificially older ages (Jercinovic and Williams 2005; Spear et al. 2009).

This study offers, therefore, the opportunity to compare the results obtained through EPMA chemical dating and those obtained by LA-ICP-MS. Indeed, two aspects differ between our data and those of Faure et al. (2010) – (i) a minimum of two generations of monazite are distinguished in our data set whereas only one was identified in Faure et al (2010), and (ii) there is a significant difference in the absolute ages obtained by both approaches.

Although Faure et al. (2010) identified “three groups of composition according to the Th/U ratio” (p. 660) for monazite grains from the La Salvetat migmatite, they interpreted them in terms of only one chemical date of 327 ± 7 Ma, reflecting the crystallization age of these monazite grains. This age is barely within error of the oldest age of 319.8 ± 1.8 Ma found in this study, although the latter is more precise. However, one more age at 298 Ma was obtained by LA-ICP-MS (with another possible event at ca. 285 Ma). In the case of the

monazite from the Laouzas granite, EPMA dating yielded only one date at 336 ± 6 Ma, whereas at least two (potentially four) were obtained by LA-ICP-MS. In this case, Faure et al. (2010) describe their monazite as patchy zoned, a feature encountered only in our younger monazite population dated at ca. 298 Ma. The fact that they did not find two age populations in their data set could be explained if they did not encounter the concentrically zoned monazite in their samples.

These differences could also be linked to the statistical treatment applied to EPMA dating. Indeed, each individual analysis bears fairly high error, but once they are all combined to calculate a total U-Th-Pb date, the resulting error becomes relatively small ($\leq 2\%$). One could therefore argue that this statistic treatment is not able to resolve different populations that are relatively close in age.

In order to test this hypothesis, we took the U, Th and Pb contents calculated for three of our samples (ES7 and ES8, this study Table 2; ES5 of Poilvet et al. 2011), and ran them into the EPMA dating add-in developed by Pommier et al. (2002) following the data treatment described in Cocherie et al. (1998) and Cocherie and Albarède (2001). In order to test the viability of our approach, we first took the data from the Montalet granite in Poilvet et al. (2011). The monazite grains in this sample yielded a single concordia age of 294 ± 1 Ma, identical to the concordia age of 294 ± 3 Ma obtained on zircon. Plotted in a Th/Pb versus U/Pb diagram (Fig. 9A), they define a similar U-Th-Pb age of 295 ± 10 Ma. This demonstrates that when dating a simple (i.e. single age) population of monazite, the results obtained by both the LA-ICP-MS and EPMA dating techniques are comparable. We then tested this approach with two other samples from this study, which gave several age populations. For sample ES7, the resulting Th/Pb versus U/Pb isochron diagram (Fig. 9B) allows to calculate a single U-Th-Pb date of 297 ± 15 Ma (MSWD = 0.28) at the centroid of the population. In this diagram, the regression line lies fairly close to the theoretical isochron,

therefore this age of ca. 297 Ma would have been considered as reliable and, therefore, unique. Yet, we know that in fact at least two ages can be calculated using the LA-ICP-MS data (ca. 319 Ma and ca. 298 Ma respectively). Although these two ages are ~ 20 Ma apart, the Th/Pb versus U/Pb isochron diagram is not able to distinguish them. If we do the same operation with monazite data from sample ES8, we also end up with a U-Th-Pb chemical age of 291 ± 8 Ma (MSWD = 0.18) at the centroid of the population (Fig. 9C) although three ages can be calculated in a conventional concordia diagram (ca. 319 Ma, 298 Ma and, maybe, 284 Ma). In this case we reached the limits of the technique as the theoretical isochron fits just within the limits of the error envelope. This does not explain however why the EPMA ages found by Faure et al. (2010) are significantly older than the ages found by LA-ICP-MS.

It is interesting to note that, with the same data set, but using the procedure described in Montel et al. (1996) where, for each individual age, the 95% confidence interval is estimated by a Monte Carlo procedure assuming U, Th and Pb content to obey a Gaussian distribution, we end up with completely different results, as the age distributions for sample ES7 yield three different date peaks at ca. 318 Ma, 302 Ma and 270 Ma (Fig. 10), which is in a good agreement with the ages found in this study.

7. Conclusion

The presence of two stages of partial melting, at ca. 320 Ma and ca. 300 Ma, confirms (i) the interpretation of the Late Carboniferous-Early Permian evolution of the Variscan belt dominated by extensional collapse, which predicts migmatization both preceding, and contemporaneous with, the onset of extension, and (ii) the interpretation of the Montagne Noire dome as an extensional gneiss dome.

We also demonstrate that EPMA dating of monazite in this type of complex poly-phased environment should be used with extreme caution. Indeed, as illustrated here, the Pb/U

and Th/U isochron statistical data treatment (Pommier et al. 2002) can sometimes fail to resolve different age populations and can, therefore, produce erroneous results.

Acknowledgments

Xavier Le Coz is acknowledged for making promptly the thin sections required for our study, Yann Lepagnet for the efficient rock crushing. Thomas Delhay for help with NanoSIMS analysis. Jean-Marc Montel and an anonymous reviewer are thanked for their constructive remarks of a previous version of this manuscript. The reviews of P. Rey and E. Oliot are acknowledged.

References

- Alabouvette B, Demange M (1993) Notice explicative, Carte géol. France (1/50 000), feuille Saint-Pons (1013). Orléans, BRGM, 123 pp
- Arthaud F (1970) Etude tectonique comparée de deux domaines hercyniens : les nappes de la Montagne Noire (France) et l'anticlinorium de l'Iglesiente (Sardaigne), Thesis, University of Montpellier, Publications USTELA Géol. Struct., 175 pp
- Arthaud F, Mattauer M, Proust F (1966) La structure et la microtectonique des nappes hercyniennes de la Montagne Noire. In: Etages tectoniques : Colloque de Neuchâtel, 18-19 avril 1966, Université de Neuchâtel, 231-243.
- Arthaud F, Matte P (1977) Late Paleozoic strike slip faulting in southern Europe and northern Africa: Result of a right-lateral shear zone between the Appalachians and the Urals. Geological Society of America Bulletin 88:1305-1320.
- Barbey P, Villaros A, Marignac C, Montel J-M (2015) Multiphase melting, magma emplacement and P-T-time path in late-collisional context: the Velay example (Massif Central, France). Bull. Soc. géol. Fr. 186(2-3):93-116

703 Becq-Giraudon JF, Van Den Driessche J (1993) Continuité de la sédimentation entre le
 704 Stéphanien et l'Autunien dans le bassin de Graissessac-Lodève (sud du Massif Central) :
 705 implications tectoniques. *Comptes Rendus de l'Académie des Sciences série 2*, 317:939-945.

706 Benard F, Moutou P, Pichavant M (1985) Phase Relations of Tourmaline Leucogranites and
 707 the Significance of Tourmaline in Silicic Magmas. *Journal of Geology* 93:271-291.

708 Blès J-L, Bonijoly C, Castaing C, Gros Y (1989) Successive post-Variscan stress fields in the
 709 French Massif Central and its borders (Western European plate): comparison with
 710 geodynamical data. *Tectonophysics* 169: 79-111.

711 Bogdanoff S, Donnot F, Ellenberger F (1984) Note explicative, Carte géol. France (1/50 000),
 712 feuille Bédarieux (988),. Orléans, BRGM, 105 pp

713 Bosse V, Boulvais P, Gautier P, Tiepolo M, Ruffet G, Devidal J-L, Cherneva Z, Gerdjikov I,
 714 Paquette J-L (2009) Fluid-induced disturbance of the monazite Th-Pb chronometer: In situ
 715 dating and element mapping in pegmatites from the Rhodope (Greece, Bulgaria). *Chemical*
 716 *Geology* 261:286-302.

717 Boutin A, de Saint Blanquat M, Poujol M, Boulvais P, de Parseval P, Rouleau C, Robert JF
 718 (2015). Succession of Permian and Mesozoic metasomatic events in the eastern Pyrenees with
 719 emphasis on the Trimouns talc-chlorite deposit. *International Journal of Earth Sciences*,
 720 doi:10.1007/s00531-015-1223-x.

721 Brun J-P, Van Den Driessche J (1994) Extensional gneiss domes and detachment fault
 722 systems: structures and kinematics. *Bulletin de la Société Géologique de France* 165:519-530.

723 Bruguier O, Becq-Giraudon JF, Champenois M, Deloule E, Ludden J, Mangin D (2003)
 724 Application of in situ zircon geochronology and accessory phase chemistry to constraining
 725 basin development during post-collisional extension: a case study from the French Massif
 726 Central. *Chemical Geology* 201:319-336.

727 Brunel M, Languet C (1997) Déformation et cinématique de mise en place du dôme de la
 728 zone axiale de la Montagne Noire: signification des nodules à quartz-sillimanite (Massif
 729 central français) [Deformation and kinematics of emplacement of the axial dome of the
 730 Montagne Noire: implications of quartz-sillimanite nodule attitudes (French Massif Central)].
 731 *Comptes Rendus de l'Académie des Sciences Paris - Series IIA - Earth and Planetary Sciences*
 732 325:517-523.

733 Burg J-P, Matte PJ (1978) A Cross Section through the French Massif Central and the Scope
734 of its Variscan Geodynamic Evolution. *Zeitschrift der Deutschen Geologischen Gesellschaft*,
735 129:429-460.

736 Burg J-P, Van Den Driessche J, Brun J-P (1994) Syn- to post-thickening extension in the
737 Variscan Belt of Western Europe: Modes and structural consequences. *Géologie de la France*
738 3:33-51.

739 Cassard D, Feybesse J-L, Lescuyer J-L (1993) Variscan crustal thickening, extension and late
740 overstacking during the Naumrian-Westphalian in the western Montagne Noire.
741 *Tectonophysics* 222: 33-53

742 Cathelineau M, Boiron M-C, Holliger P, Poty B (1990). Metallogenesis of the French part of
743 the Variscan orogen. Part II: Time-space relationships between U, Au and Sn-W ore
744 deposition and geodynamic events — mineralogical and U-Pb data. *Tectonophysics* 177:59–
745 79.

746 Charles N, Faure M, Chen Y (2009) The Montagne Noire migmatitic dome emplacement
747 (French Massif Central): new insights from petrofabric and AMS studies. *Journal of*
748 *Structural Geology* 31:1423-1440.

749 Cocherie A, Legendre O, Peucat J-J, Kouamelan AN (1998) Geochronology of polygenetic
750 monazites constrained by in situ electron microprobe Th–U–total lead determination;
751 implications for lead behaviour in monazite. *Geochimica Cosmochimica Acta* 62:2475 –
752 2497.

753 Cocherie A, Albarède F (2001) An improved U–Th–Pb age calculation for electron
754 microprobe dating of monazite. *Geochimica et Cosmochimica Acta* 65:4509-4522.

755 Didier A, Bosse V, Boulvais P, Bouloton J, Paquette J-L, Montel J-M, Devidal J-L (2013)
756 Disturbance versus preservation of U-Th-Pb ages in monazite during fluid-rock interaction:
757 textural, chemical and isotopic in situ study in microgranites (Velay Dome, France).
758 *Contributions to Mineralogy and Petrology* 165:1051-1072

759 Demange M (1982) Etude géologique du massif de l'Agout, Montagne Noire, France, Thèse
760 d'Etat, University Paris 6, 1050 pp

761 Demange M, Guérangé-Lozes J, Guérangé B (1995) Notice explicative, Carte géol. France
762 (1/50 000), feuille Lacane (987). Orléans, BRGM, 153 pp

763 Doublier M P, Potel S, Wemmer K (2015) The tectono-metamorphic evolution of the very
 764 low-grade hangingwall constrains two-stage gneiss dome formation in the Montagne Noire
 765 (Southern France). *Journal of metamorphic Geology* 33: 71-89
 766 Echtler H (1990) Geometry and kinematics of recumbent folding and low-angle detachment
 767 in the Pardailhan nappe (Montagne Noire, Southern French Massif Central). *Tectonophysics*
 768 177: 109-123
 769 Echtler H, Malavieille M (1990) Extensional tectonics, basement uplift and Stephano-Permian
 770 collapse basin in a late Variscan metamorphic core complex (Montagne Noire, Southern
 771 Massif Central). *Tectonophysics* 177: 125-138
 772 Faure M, Cottureau N (1988) Données cinématiques sur la mise en place du dôme
 773 migmatitique carbonifère moyen de la zone axiale de la Montagne noire (Massif central
 774 français). *Comptes rendus de l'Académie des Sciences* 307: 1787-1794
 775 Faure M, Cocherie A, Bé Mézème E, Charles N, Rossi P (2010) Middle Carboniferous crustal
 776 melting in the Variscan Belt: New insights from U-Th-Pb_{tot} monazite and U-Pb zircon ages of
 777 the Montagne Noire Axial Zone (southern French Massif Central). *Gondwana Research*
 778 18:653-673.
 779 Foster G, Kinny P, Vance D, Prince C, Harris N (2000) The significance of monazite U–Th–
 780 Pb age data in metamorphic assemblages; a combined study of monazite and garnet
 781 chronometry. *Earth and Planetary Science Letters* 181:327-340.
 782 Franke W, Doublier MP, Klama K, Potel S, Wemmer K (2011) Hot metamorphic core
 783 complex in a cold foreland. *International Journal of Earth Sciences* 100: 753-785
 784 Gardés E, Montel J-M, Seydoux-Guillaume A-M, Wirth R (2007) Pb diffusion in monazite:
 785 New constraints from the experimental study of $Pb^{2+} \rightleftharpoons Ca^{2+}$ interdiffusion. *Geochimica et*
 786 *Cosmochimica Acta* 71:4036-4043.
 787 Gasquet D, Bertrand J-M, Paquette J-L, Lehmann J, Ratzov G, De Ascensão Guedes R,
 788 Tiepolo M, Boullier AM, Scaillet S, Nomade S (2010) Miocene to Messinian deformation and
 789 hydrothermalism in the Lauzière Massif (French Western Alps): New U–Th–Pb and Argon
 790 ages. *Bulletin de la Société Géologique de France* 181:227–241.
 791 Hollister LS (1993) The role of melt in the uplift and exhumation of orogenic belts. *Chem.*
 792 *Geol.* 108:31-48

793 Holtz F, Johannes W (1994) Maximum and minimum water contents of granitic melts:
 794 implications for chemical and physical properties of ascending magmas. *Lithos* 32:149-159
 795 Holtz F, Johannes W, Tamic N, Behrens H (2001) Maximum and minimum water contents of
 796 granitic melts generated in the crust: reevaluation and implications. *Lithos* 56:1-14
 797 Hurai V, Paquette J-L, Huraiová M, Konečný P (2010) U-Th-Pb geochronology of zircon and
 798 monazite from syenite and pincinite xenoliths in Pliocene alkali basalts of the intra-
 799 Carpathian back-arc basin. *Journal of Volcanology and Geothermal Research* 198:275-287.
 800 Jackson SE, Pearson NJ, Griffin WL, Belousova EA (2004) The application of laser ablation-
 801 inductively coupled plasma-mass spectrometry to in situ U-Pb zircon geochronology.
 802 *Chemical Geology* 211:47-69.
 803 Jercinovic MJ, Williams ML (2005) Analytical perils (and progress) in electron microprobe
 804 trace elements analysis applied to geochronology: Background, interferences and beam
 805 irradiation effects. *American Mineralogist* 90:526-546.
 806 Jourdan F, Renne PR (2007) Age calibration of the Fish Canyon sanidine $^{40}\text{Ar}/^{39}\text{Ar}$ dating
 807 standard using primary K-Ar standards. *Geochimica Cosmochimica Acta* 71:387-402.
 808 Jourdan F, Verati C, Féraud G (2006) Intercalibration of the Hb3gr $^{40}\text{Ar}/^{39}\text{Ar}$ dating standard.
 809 *Chemical Geology* 231:77-189.
 810 Kelsey DE, Clark C, Hand M (2008) Thermobarometric modelling of zircon and monazite
 811 growth in melt-bearing systems: examples using model metapelitic and metapsammitic
 812 granulites. *Journal of Metamorphic Geology* 26:199-212.
 813 Ludwig KR (1998) On the treatment of concordant uranium-lead ages. *Geochimica et*
 814 *Cosmochimica Acta* 62:665-676.
 815 Ludwig KR (2001) User's manual for Isoplot/Ex Version 2.49, a geochronological toolkit for
 816 Microsoft Excel. Spec Publ., 1a. Berkeley Geochronological Center, Berkeley, USA.
 817 Maluski H, Costa S, Echtler H (1991) Late Variscan tectonic evolution by thinning of earlier
 818 thickened crust. An ^{40}Ar - ^{39}Ar study of the Montagne Noire, southern Massif Central, France.
 819 *Lithos* 26:287-304.
 820 Matte P, Lancelot J, Mattauer (1998) The Montagne Noire Axial Zone is not an extensional
 821 metamorphic core complex but a compressional post-nappe anticline with an anatectic core.
 822 *Geodinamica Acta* 11: 3-22

823 Ménéard G, Molnar P (1988) Collapse of a Hercynian Tibetan Plateau into a late Paleozoic
824 European Basin and Range province. *Nature* 334:235-237.

825 Montel J-M, Marignac C, Barbey P, Pichavant M (1992) Thermobarometry and granite
826 genesis: the Hercynian low-P high-T Velay anatectic Dome (French Massif Central). *Journal*
827 *of Metamorphic Geology* 10:1-15.

828 Montel J, Foret S, Veschambre M, Nicollet C, Provost A (1996) Electron microprobe dating
829 of monazite. *Chemical Geology* 131:37–53.

830 Mougéot R, Respaut J-P, Ledru P, Marignac C (1997) U-Pb geochronology on accessory
831 minerals of the Velay anatectic Dome (French Massif Central). *European Journal of*
832 *Mineralogy* 9:141-156.

833 Paquette J-L, Tiepolo M (2007) High resolution (5 μm) U–Th–Pb isotopes dating of monazite
834 with excimer laser ablation (ELA)-ICPMS. *Chemical Geology* 240:222–237.

835 Pitra P, Ballèvre M, Ruffet G (2010) Inverted metamorphic field gradient towards a Variscan
836 suture zone (Champtoceaux Complex, Armorican Massif, France). *Journal of Metamorphic*
837 *Geology* 28:183-208.

838 Pitra P, Poujol M, Van Den Driessche J, Poilvet J-C, Paquette J-L (2012) Early Permian
839 extensional shearing of an Ordovician granite: The Saint-Eutrope , "C/S-like" orthogneiss
840 (Montagne Noire, French Massif Central). *Comptes Rendus Geoscience* 344:377-384.

841 Pochat S, Van Den Driessche J (2011) Filling sequence in Late Paleozoic continental basins;
842 A chimera of climate change. A new light shed given by the Graissessac-Lodève basin (SE
843 France). *Palaeogeography, Palaeoclimatology, Palaeoecology* 302:170-186.

844 Poilvet J-C, Poujol M, Pitra P, Van Den Driessche J, Paquette J-L (2011) The Montalet
845 granite, Montagne Noire, France: An early Permian syn-extensional pluton as evidenced by
846 new U-Th-Pb data on zircon and monazite. *Comptes Rendus Geoscience* 343:454-461.

847 Poitrasson F, Chenery S, Shepherd TJ (2000) Electron microprobe and LA-ICP-MS study of
848 monazite hydrothermal alteration: Implications for U-Th-Pb geochronology and nuclear
849 ceramics. *Geochimica and Cosmochimica Acta* 64:3283-3297.

850 Pommier A, Cocherie A, Legendre O (2002) EPMA Dating User's manual: Age calculation
851 from electron probe microanalyser measurements of U–Th–Pb. BRGM, 9 pp.

852 Rabin M, Trap P, Carry N., Fréville K., Centi-Tok B, Lobjoie C, Goncalves P, Marquer D
853 (2015) Strain partitioning along the anatectic front in the Variscan Montagne Noire massif
854 (southern French Massif Central). *Tectonics* 34 :doi:10.1002/2014TC003790.

855 Renne PR, Balco G, Ludwig RL, Mundil R, Min K (2011) Response to the comment by W.H.
856 Schwarz et al. on “Joint determination of $(40)\text{K}$ decay constants and $(40)\text{Ar}^*/(40)\text{K}$ for the Fish
857 Canyon sanidine standard, and improved accuracy for $(40)\text{Ar}/(39)\text{Ar}$ geochronology” by PR
858 Renne et al. (2010). *Geochimica et Cosmochimica Acta* 75:5097–5100.

859 Renne PR, Mundil R, Balco G, Min K, Ludwig RL (2010) Joint determination of ^{40}K decay
860 constants and $^{40}\text{Ar}^*/^{40}\text{K}$ for the Fish Canyon sanidine standard, and improved accuracy for
861 $^{40}\text{Ar}/^{39}\text{Ar}$ geochronology. *Geochimica et Cosmochimica Acta* 74:5349–5367.

862 Rey PF, Teyssier C, Whitney DL (2011) Viscous collision in channel explains double domes
863 in metamorphic core complexes. *Geology* 39: 387-390

864 Roddick JC (1983) High precision intercalibration of $^{40}\text{Ar}/^{39}\text{Ar}$ standards. *Geochimica et*
865 *Cosmochimica Acta* 47:887–898.

866 Roger F, Respaut J-P, Brunel M, Matte P, Paquette J-L (2004) U-Pb dating of Augen
867 orthogneisses from the Axial Zone of the Montagne Noire (Southern Massif Central): new
868 witness of Ordovician magmatism into the Variscan Belt. *Comptes Rendus Geoscience*
869 336:19-28.

870 Roger F, Teyssier C, Respaut J-P, Rey PF, Jolivet M, Whitney DL, Paquette J-L, Brunel M
871 (2015) Timing of formation and exhumation of the Montagne Noire double dome, French
872 Massif Central. *Tectonophysics* 640-641:53-69

873 Rubatto D, Williams IS, Buick IS (2001) Zircon and monazite response to prograde
874 metamorphism in the Reynolds Range, central Australia. *Contributions to Mineralogy and*
875 *Petrology* 140:458-468.

876 Ruffet G, Féraud G, Amouric M (1991) Comparison of $^{40}\text{Ar}/^{39}\text{Ar}$ conventional and laser dating
877 of biotites from the North Trégor Batholith. *Geochimica et Cosmochimica Acta* 55:1675–1688.

878 Ruffet G, Féraud G, Ballèvre M, Kiénast JR (1995) Plateau ages and excess argon on phengites:
879 a $^{40}\text{Ar}/^{39}\text{Ar}$ laser probe study of alpine micas (Sesia zone). *Chemical Geology* 121:327–343.

880 Seydoux-Guillaume A-M, Paquette J-L, Wiedenbeck M, Montel J-M, Heinrich W (2002)
881 Experimental resetting of the U-Th-Pb systems in monazite. *Chemical Geology* 191:165-181.

882 Soula JC, Debat P, Brusset S, Bessière G, Christophoul F, Déramond J (2001) Thrust-related,
883 diapiric, and extensional doming in a frontal orogenic wedge: exemple of the Montagne noire,
884 Southern French Hercynian Belts. *Journal of Structural Geology* 23: 1677-1699

885 Spear FS, Pyle JM (2010) Theoretical modeling of monazite growth in a low-Ca metapelite.
886 *Chemical Geology* 273:111-119.

887 Spear FS, Pyle JM, Cherniak D (2009) Limitations of chemical dating of monazite, *Chemical*
888 *Geology* 266:218-230.

889 Taner MF, Martin RF (1993) Significance of dumortierite in an aluminosilicate-rich alteration
890 zone, Louvicourt, Quebec. *Canadian Mineralogist* 31:137-146.

891 Tartèse R, Ruffet G, Poujol M, Boulvais P, Ireland TR (2011) Simultaneous resetting of the
892 muscovite K-Ar and monazite U-Pb geochronometers: a story of fluids. *Terra Nova* 23:390-
893 398.

894 Tartèse R, Boulvais P, Poujol M, Chevalier T, Paquette J-L, Ireland TR, Deloule E (2012)
895 Mylonites of the South Armorican Shear Zone: Insights for crustal-scale fluid flow and water-
896 rock interaction processes. *Journal of Geodynamics* 56-57:86–107.

897 Thompson AB (2001) Clockwise P-T paths for crustal melting and H₂O recycling in granite
898 source regions and migmatite terrains. *Lithos* 56:33-45

899 Turner G, Huneke JC, Podosek FA, Wasserburg GJ (1971) ⁴⁰Ar/³⁹Ar ages and cosmic ray
900 exposure age of Apollo 14 samples. *Earth and Planetary Science Letters* 12:19–35.

901 Van Den Driessche J, Brun J-P (1989) Un modèle cinématique de l'extension paléozoïque
902 supérieur dans le sud du Massif Central. *Comptes Rendus de l'Académie des Sciences série 2*
903 309:1607-1613.

904 Van Den Driessche J, Brun J-P (1992) Tectonic evolution of the Montagne Noire (French
905 Massif Central): a model of extensional dome. *Geodinamica Acta* 5:85-99.

906 Van Den Driessche J, Pitra P (2012) Viscous collision channel explains double dome in
907 metamorphic core complexes: Comment. *Geology* 40: e279

908 Velichkin VI, Vlasov BP (2011) Domal structures and hydrothermal uranium deposits of the
909 Erzgebirge, Saxony, Germany. *Geol. Ore Depos.* 53:74–83.

910 Wiedenbeck M, Allé P, Corfu F, Griffin WL, Meier M, Oberli F, von Quadt A, Roddick JC,
911 Spiegel W (1995) Three natural zircon standards for U–Th–Pb, Lu–Hf, trace element and
912 REE analyses. *Geostandard Newsletter* 19:1–23.

913 Williams ML, Jercinovic MJ, Harlov DE, Budzyn Hetherington CJ (2011) Resetting monazite
914 ages during fluid-related alteration. *Chemical Geology* 283:218-225.

915

Table and Figure captions:

Figure 1. Structural map of the southern French Massif Central (MC) showing the relationships between the Montagne Noire gneiss dome, the Stephanian-Permian basins, and the Variscan thrusts and nappes (modified after Brun and Van Den Driessche, 1994). 7, 8: locations of the samples ES7 and ES8, respectively, Af: St. Affrique basin, G: Graissessac basin, L: Laouzas granite, Lo: Lodève basin P: Col de Picotalen (location of the sample of the Montalet syntectonic leucogranite, ES5, Poilvet et al. 2011), V: Vialais granite. Inset shows the location of the study area within the European Variscan belt (modified from Pitra et al. 2010). A - Alps, AM - Armorican Massif, BM - Bohemian Massif, MC - Massif Central. B - Teplá-Barrandian, Mo - Moldanubian, ST - Saxothuringian, RH - Rhenohercynian. L: Lyon; M: Montpellier; R: Rennes.

Figure 2. (a) Outcrop photograph of the Laouzas granite (ES7). Dark spots are clusters of cordierite, the elongated object in the lower central part is a biotite-rich schlier. (b-c) Microphotographs of the granite. Note the presence of subhedral, partly altered crystals of plagioclase (pl) and K-feldspar (kfs), partly pinitised crystals of cordierite (cd), and late crystals of dumortierite (dum), andalusite (and) and muscovite (mu), and the clear rim around altered plagioclase core. (d) Outcrop photograph of the banded La Salvetat migmatite (ES8). Rare garnet crystals are shown by arrows. (e-f) Microphotographs of the migmatite leucosome. Interstitial brown-blue tourmaline is located between subhedral, partly altered crystals of feldspars and anhedral quartz (e). Plagioclase crystals are partly replaced by clinozoisite (tiny high-relief crystals), biotite contains prehnite (prh) and/or clay minerals parallel to the (001) cleavage; late muscovite is also present (f).

Figure 3: Cathodoluminescence images of some of the zircon grains dated in this study: A: Laouzas granite; B and C: La Salvetat migmatite. The white circle represents the spot analysis and the number corresponds to the $^{207}\text{Pb}/^{206}\text{Pb}$ age obtained. Zr number corresponds to the grain number in Table 1.

Figure 4: Summary of the geochronological results. In all diagram, N refers to the number of analyses. Grey ellipses correspond to the data used to calculate the concordia ages. A and C: Tera-Wasserburg $^{207}\text{Pb}/^{206}\text{Pb}$ versus $^{238}\text{U}/^{206}\text{Pb}$ concordia diagram for the zircon grains analyzed in the Laouzas granite (A) and the La Salvetat migmatite (C). B and D: $^{206}\text{Pb}/^{238}\text{U}$

versus $^{208}\text{Pb}/^{232}\text{Th}$ diagram for the monazite analyzed in the Laouzas granite (B) and the La Salvetat migmatite (D). E: Relative probability plot of $^{207}\text{Pb}/^{206}\text{Pb}$ dates for all the more than 90% concordant zircon grains obtained in this study. F: Relative probability plots for all the monazite $^{206}\text{Pb}/^{238}\text{U}$ dates obtained in this study. G: Relative probability plots for all the monazite $^{208}\text{Pb}/^{232}\text{Th}$ dates obtained in this study. H: ^{40}Ar - ^{39}Ar spectra of muscovite from samples ES5, ES7 and ES8. The error bars for each temperature steps are at the 1σ level. The errors in the J-values are not included. Plateau age error is at the 2σ level.

Figure 5: Top picture: Backscattered electron image of the Type 1 monazite from sample ES7 (i.e. ca. 318 Ma). White circle represents the spot analysis and has a diameter of 7 microns. Date refers to the $^{208}\text{Pb}/^{232}\text{Th}$ individual date. M number refers to the grain number in Table 2. White square corresponds to the location of the NanoSIMS elemental images (8 bottom pictures).

Figure 6: Top picture: Backscattered electron image of the Type 2 monazite from sample ES7 (i.e. ca. 294 Ma). White circle represents the spot analysis and has a diameter of 7 microns. Date refers to the $^{208}\text{Pb}/^{232}\text{Th}$ individual date. M number refers to the grain number in Table 2. White square corresponds to the location of the NanoSIMS elemental images (8 bottom pictures).

Figure 7: Top picture: Backscattered electron image of the first group of monazite grains (i.e. ca. 319 Ma) from sample ES8. White circle represents the spot analysis and has a diameter of 7 microns. Date refers to the $^{208}\text{Pb}/^{232}\text{Th}$ date. M number refers to the grain number in Table 2. White square corresponds to the location of the NanoSIMS elemental images (8 bottom pictures).

Figure 8: Top picture: Backscattered electron image of the second group of monazite grains (i.e. ca. 298 Ma) from sample ES8. White circle represents the spot analysis and has a diameter of 7 microns. Date refers to the $^{208}\text{Pb}/^{232}\text{Th}$ date. M number refers to the grain number in Table 2. White square corresponds to the location of the NanoSIMS elemental images (8 bottom pictures).

Figure 9: Th/Pb versus U/Pb plots using data for the monazite grains from the Montalet granite (A; from Poilvet et al. 2011), the Laouzas granite (B) and the La Salvetat migmatite

984 (C). For all the diagrams, ages obtained by LA-ICP-MS (this study) are given for comparison.
985 n refers to the number of analyses plotted in the diagrams. For more explanation on these
986 plots see Cocherie and Albarède (2001).

987

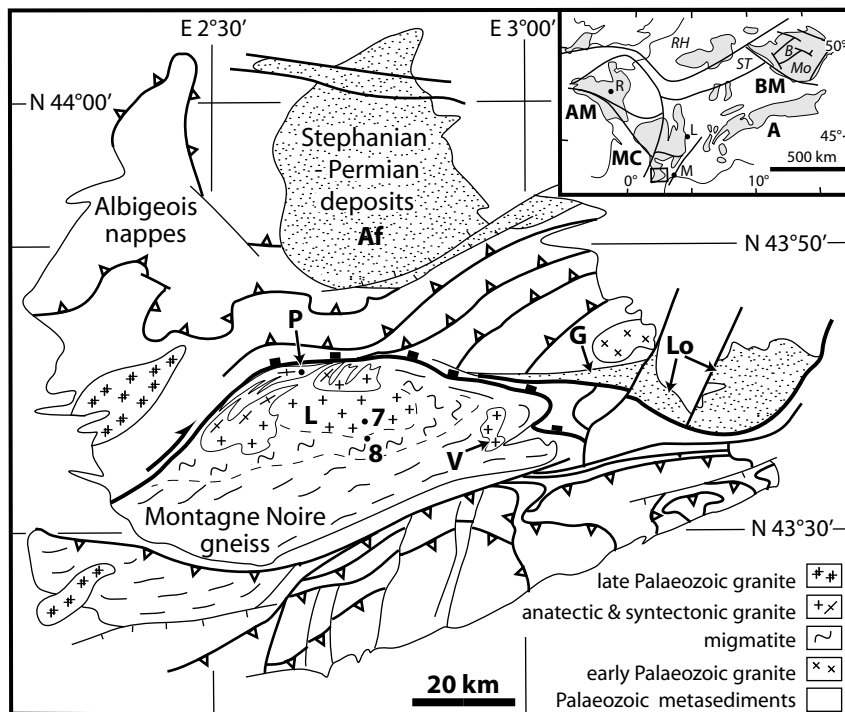
988 Figure 10: Weighted-histogram representation of the data acquired in this study for sample
989 ES7 following the statistical 1D data treatment of Montel et al (1996) for EPMA dating. For
990 more explanation on this plot see Montel et al. (1996).

991

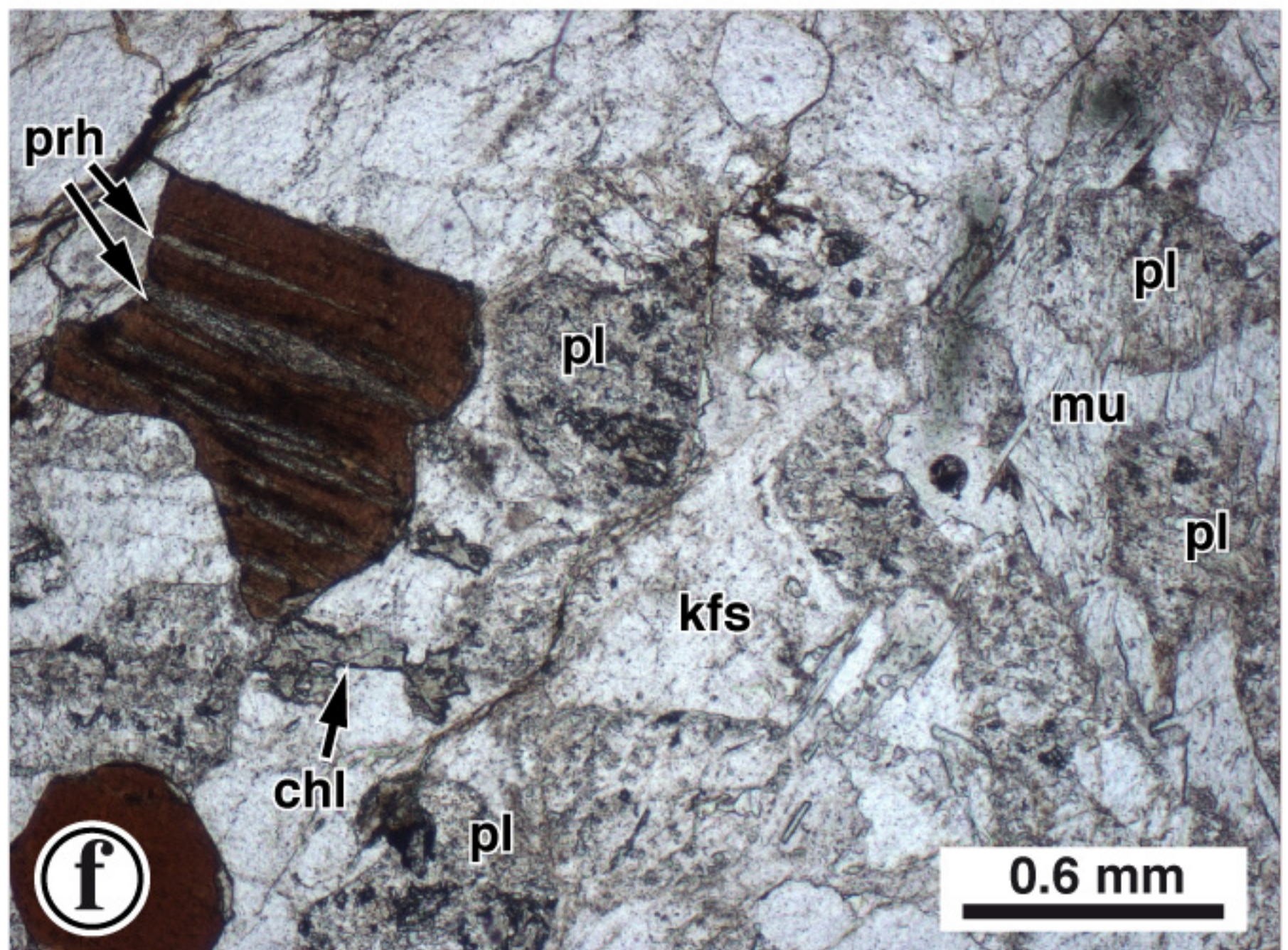
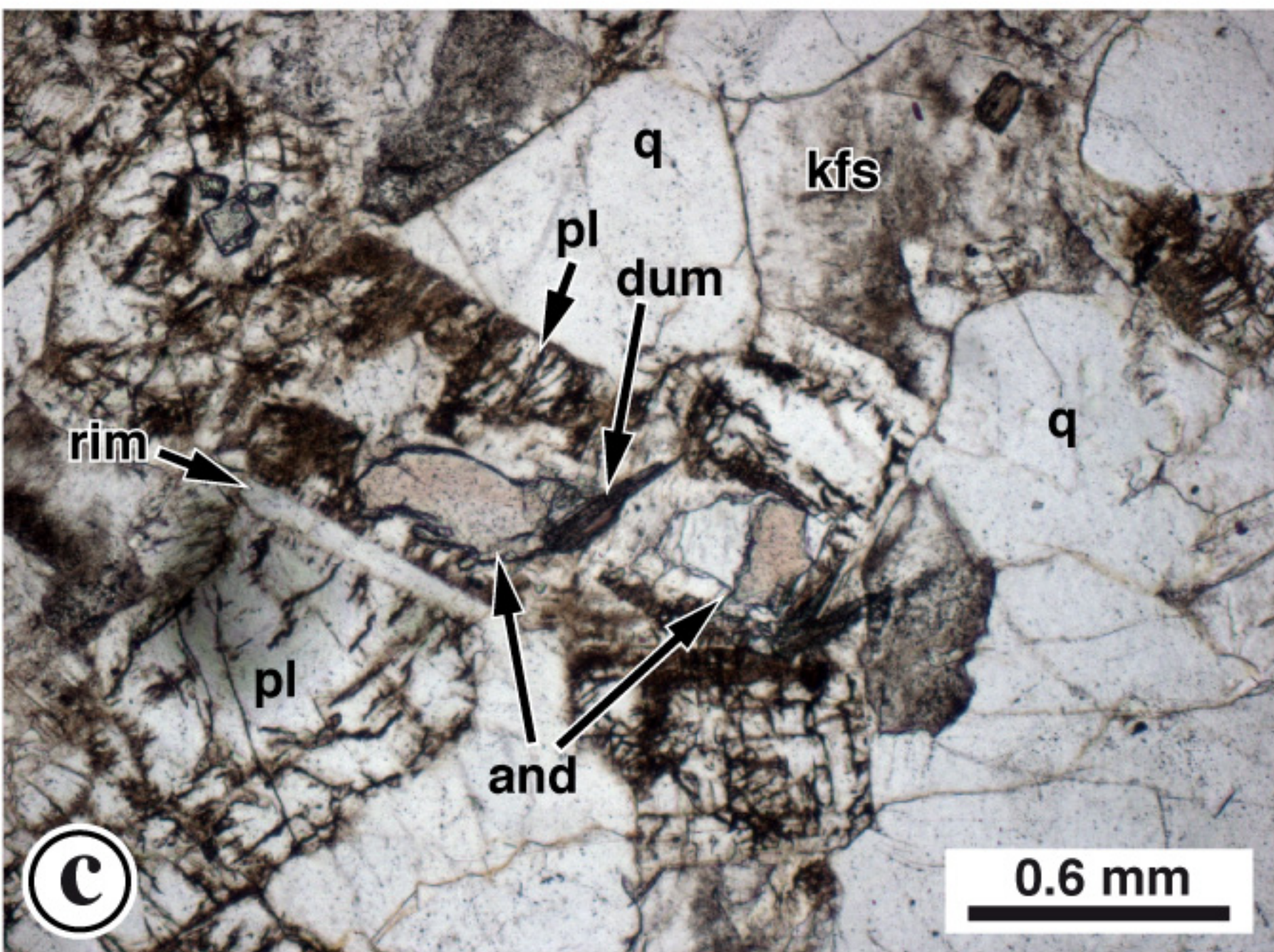
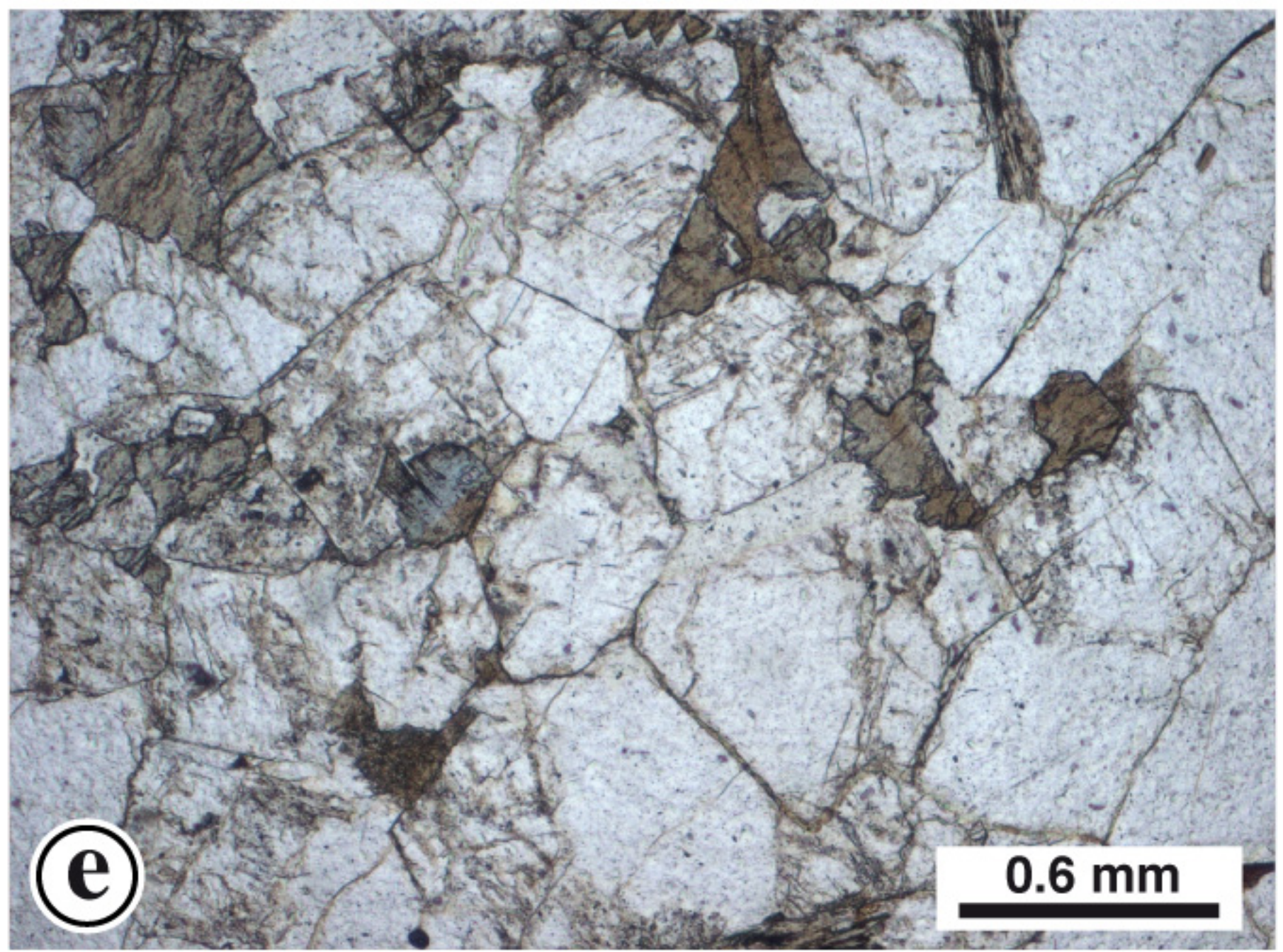
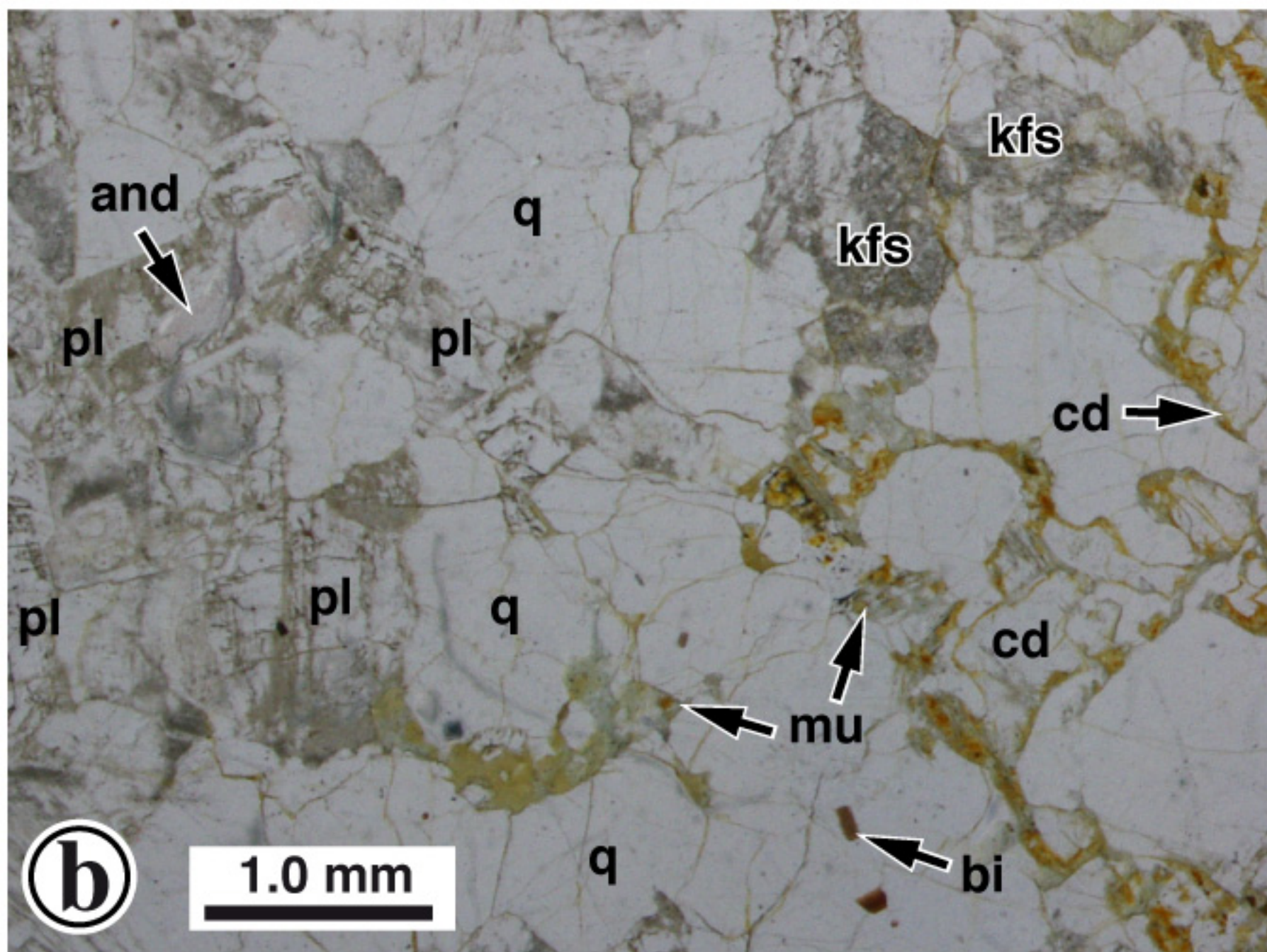
992 Table 1: U-Th-Pb LA-ICP-MS data for the zircon grains from sample ES7 and ES8. Errors
993 are reported at 1 sigma.

994

995 Table 2: U-Th-Pb LA-ICP-MS data for the monazite grains from sample ES7 and ES8. Errors
996 are reported at 1 sigma.



Poujol et al.: Fig. 1



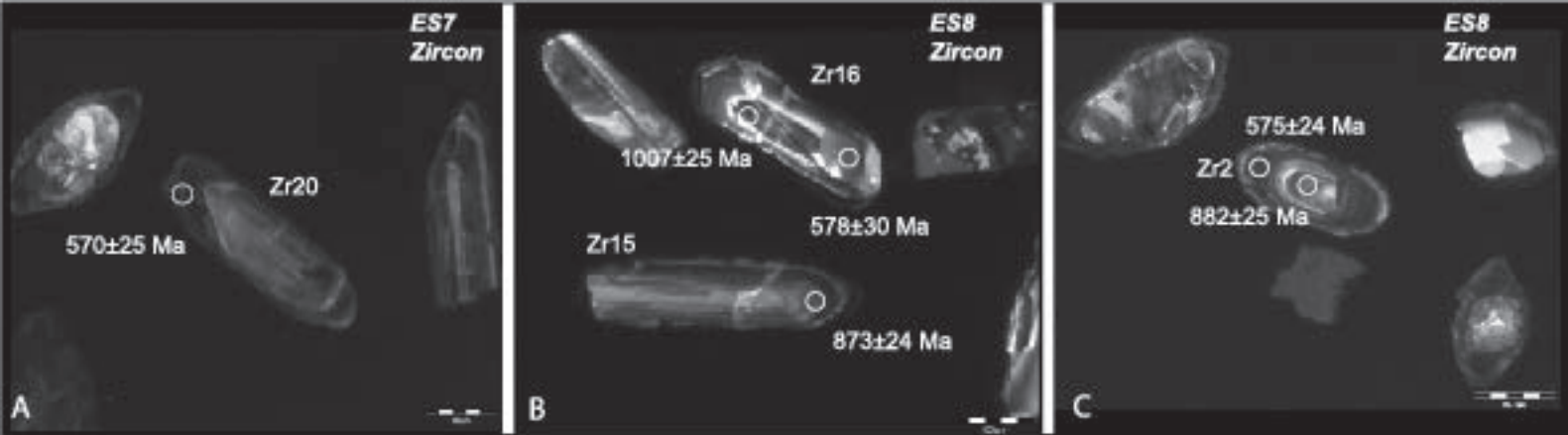
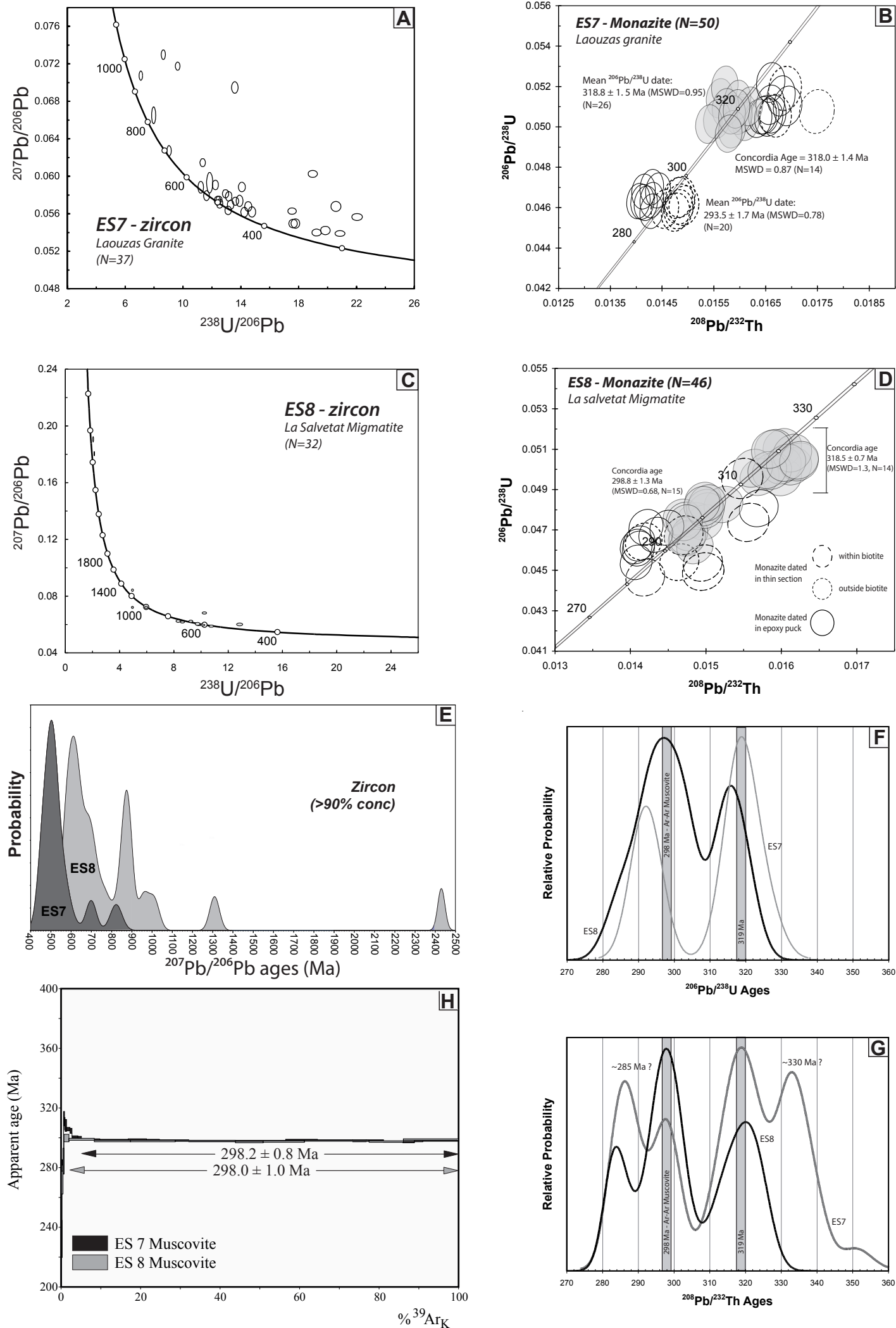
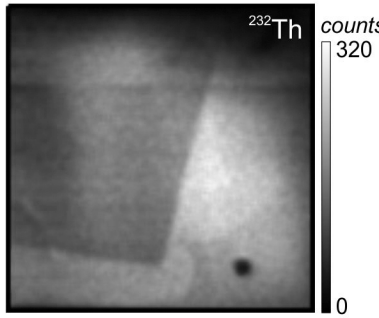
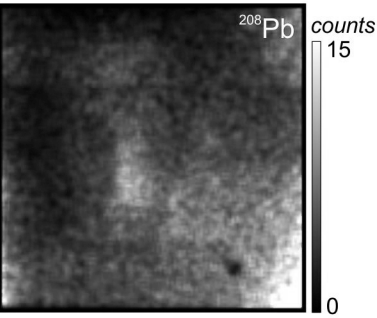
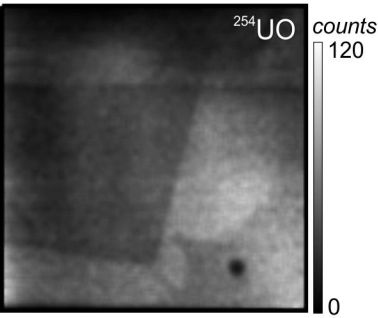
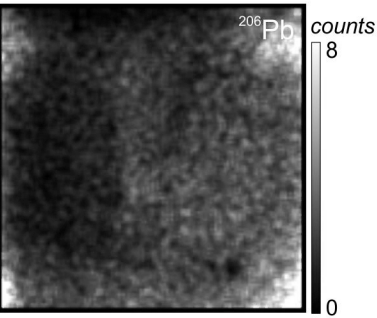
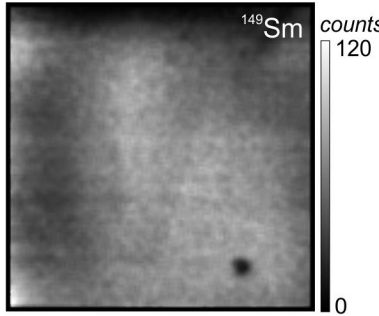
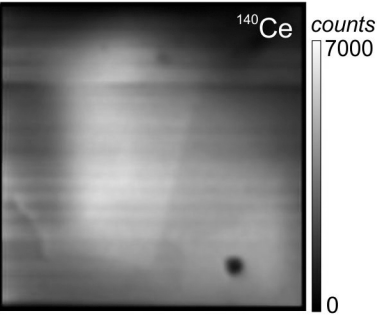
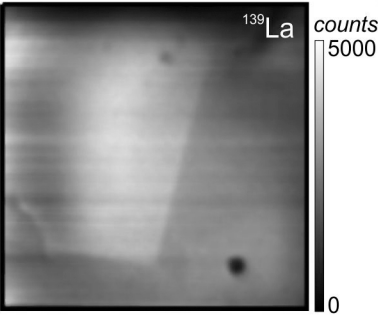
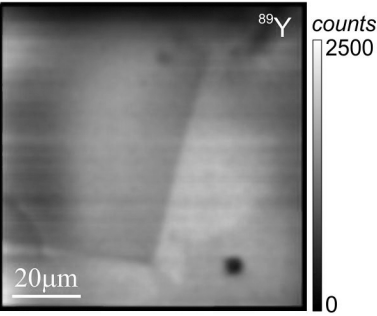
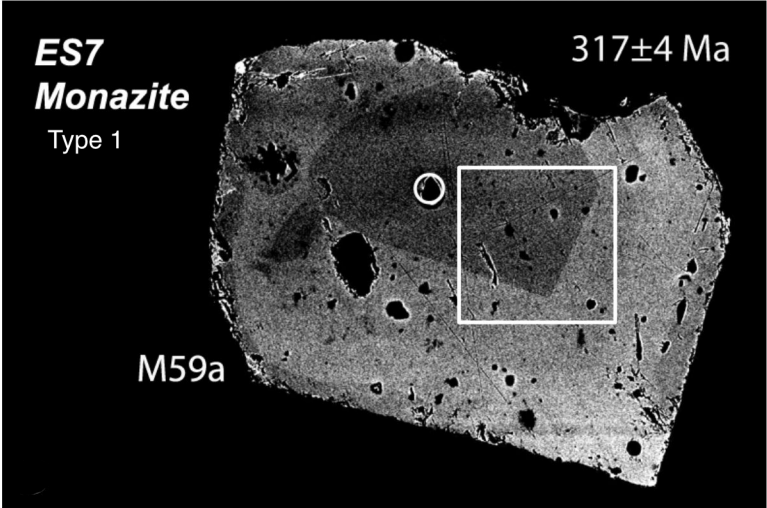
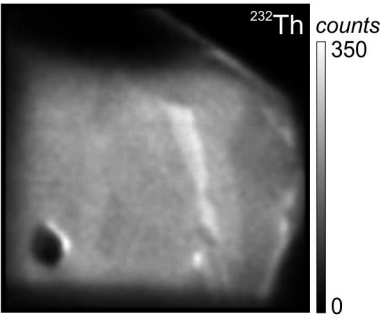
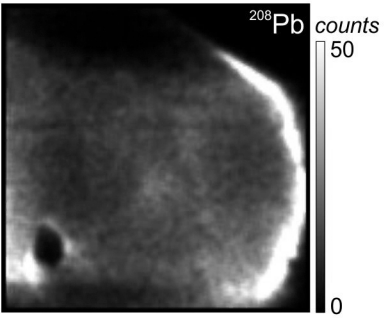
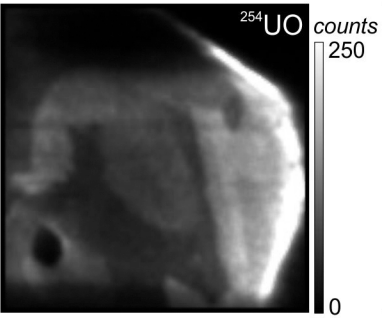
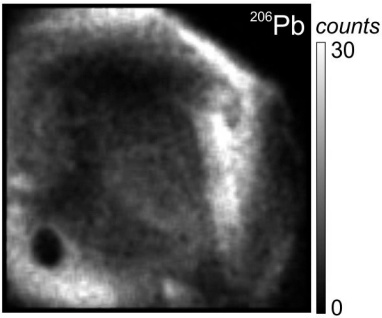
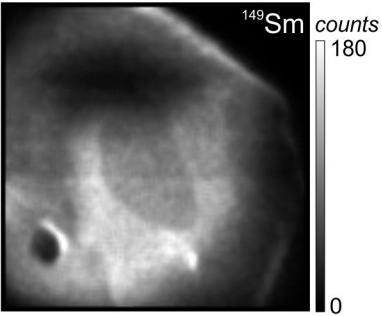
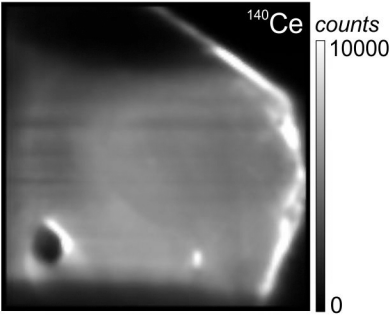
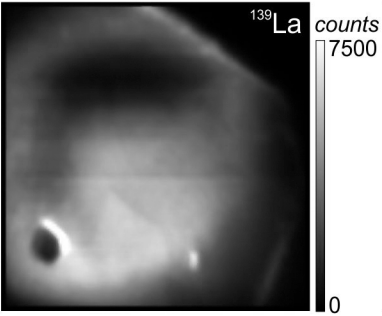
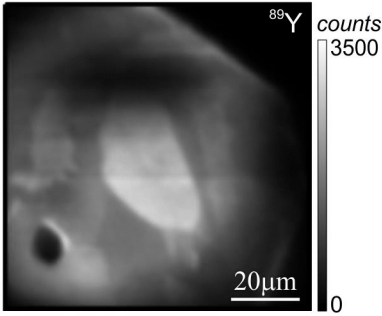
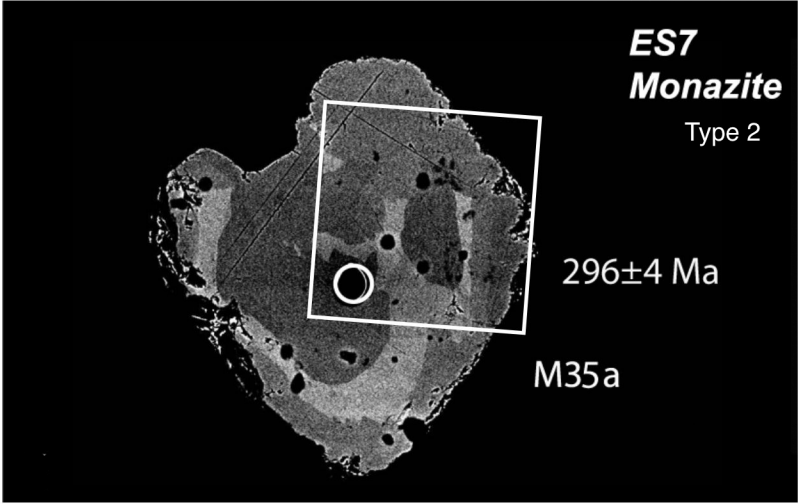
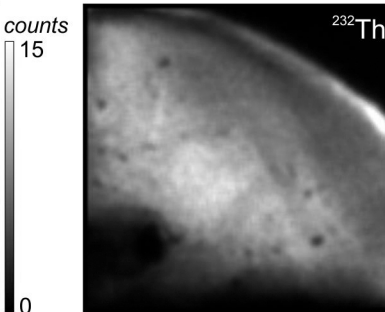
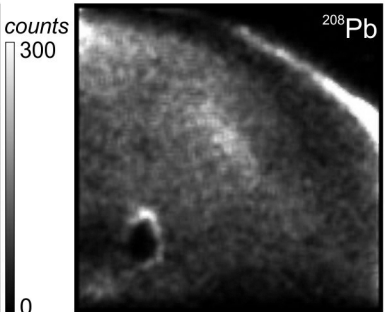
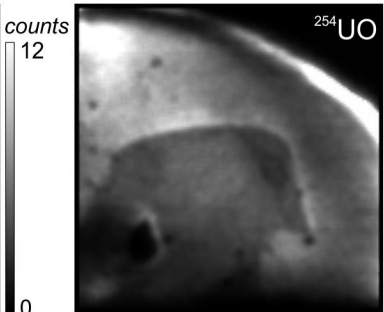
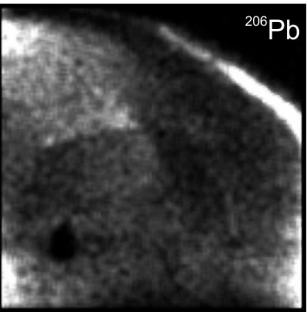
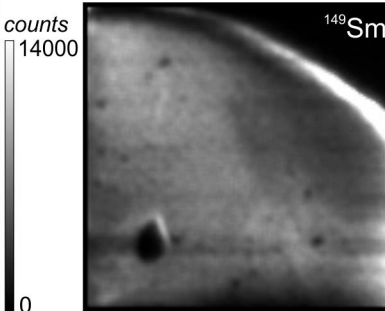
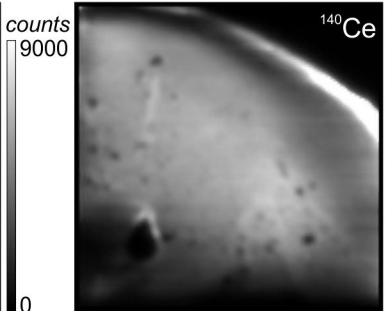
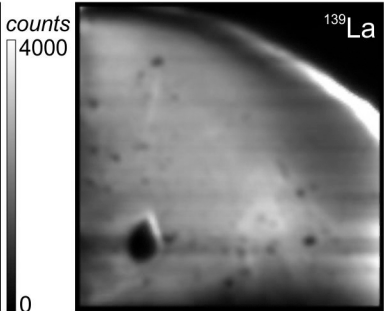
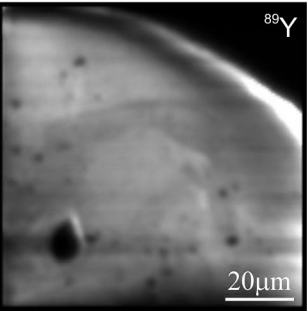
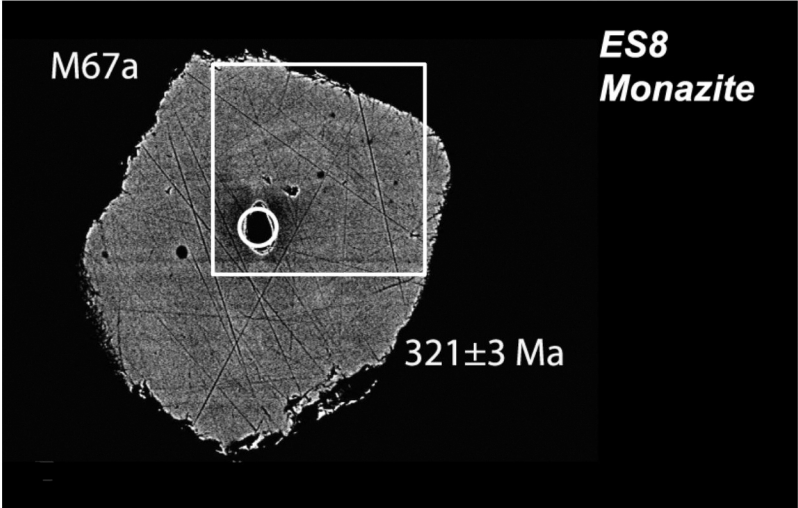


Figure 3: Poujol et al.









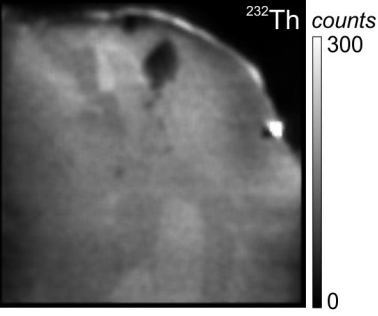
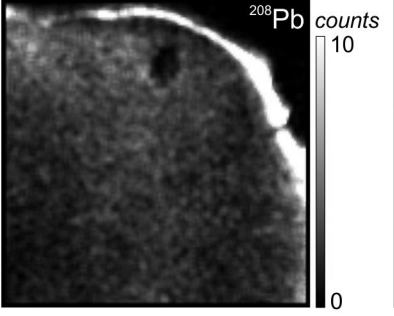
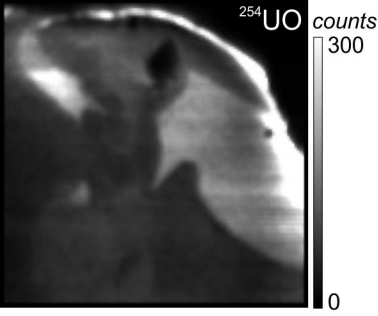
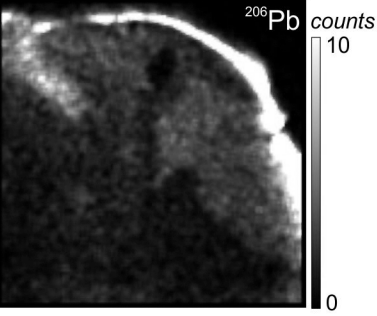
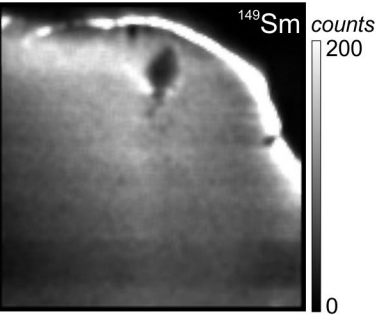
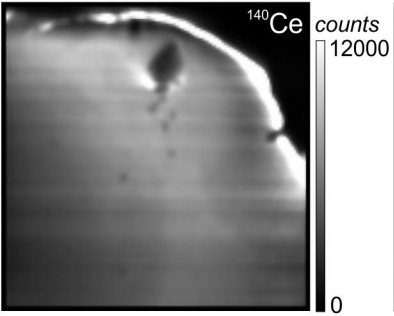
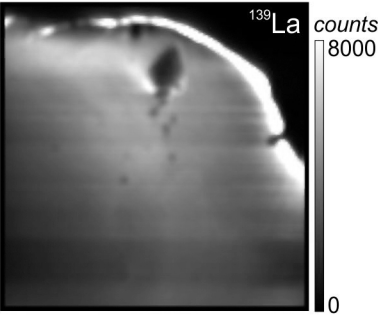
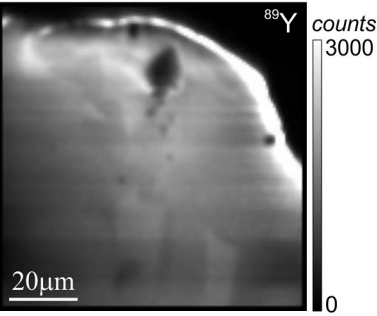
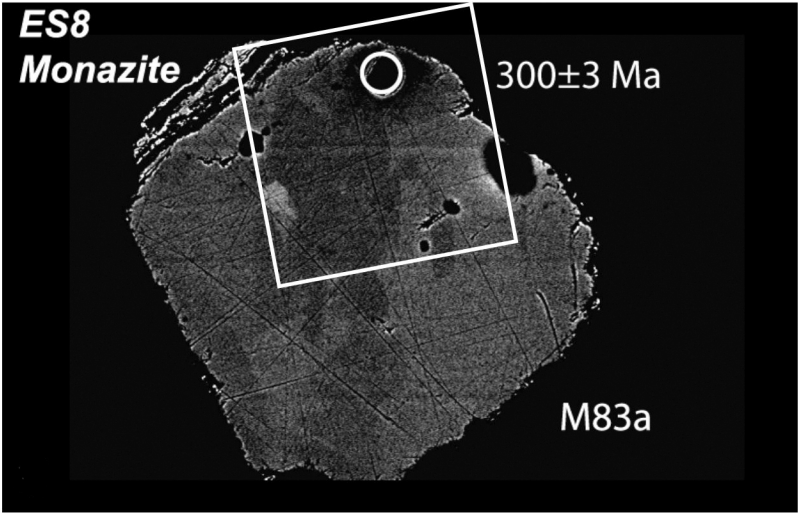


Figure 9: Poujol et al.

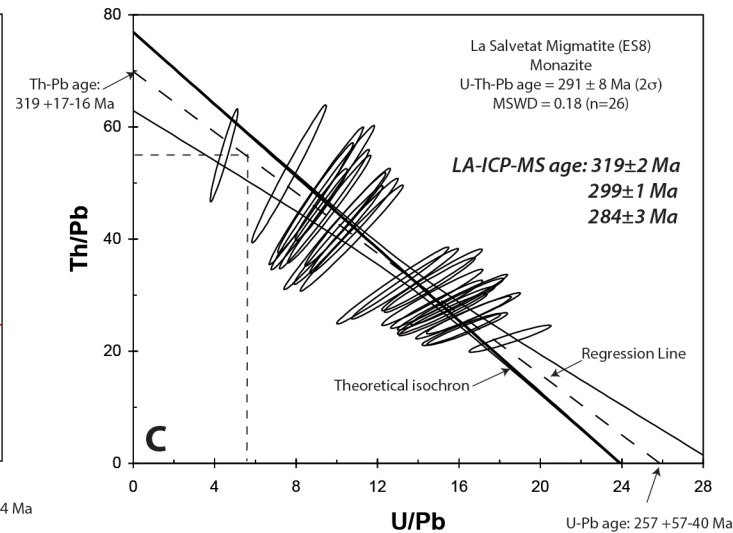
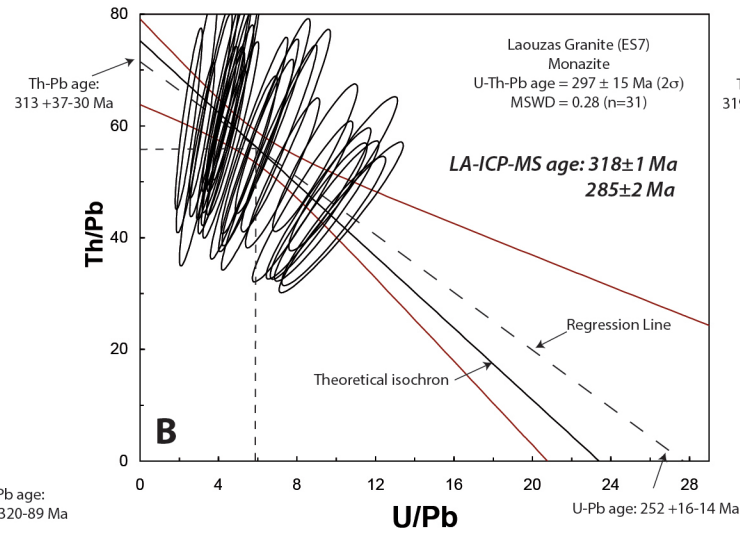
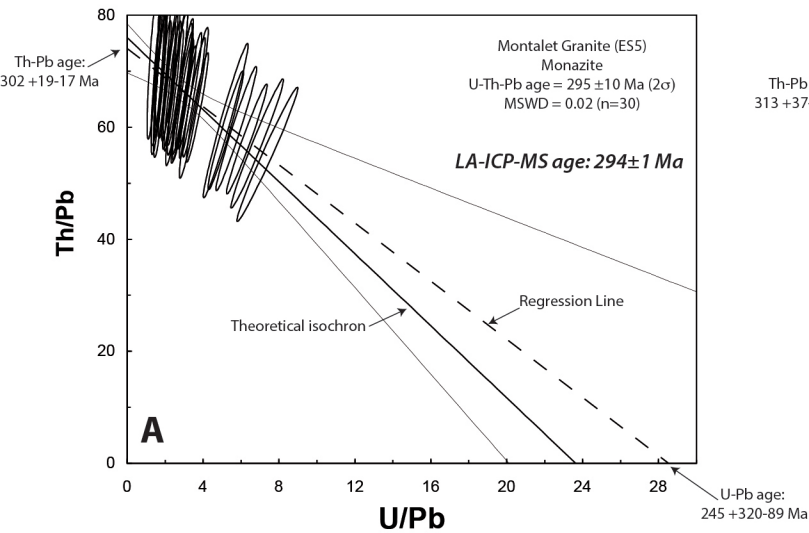
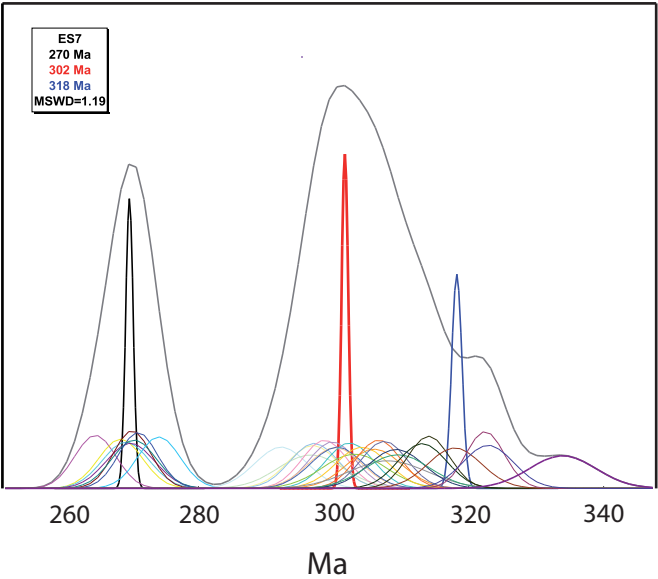


Figure 10: Poujol et al.



grain (zircon)	[Pb] (ppm)	[U] (ppm)	Th/U	²⁰⁷ Pb/ ²³⁵ U		²⁰⁶ Pb/ ²³⁸ U		²⁰⁷ Pb/ ²⁰⁶ Pb		Rho	Ages				Conc. (%)
				± 1 σ	± 1 σ	± 1 σ	± 1 σ	²⁰⁷ Pb/ ²³⁵ U	²⁰⁶ Pb/ ²³⁸ U		²⁰⁷ Pb/ ²⁰⁶ Pb	± 1 σ			
ES 7 Laouzas Granite															
1.2c	31	509	0.19	0.705	0.009	0.0736	0.0008	0.0695	0.0008	0.88	542	458	913	25	50
2.1c	39	376	0.43	1.166	0.014	0.1158	0.0013	0.0730	0.0008	0.92	785	707	1014	23	70
2.2c	104	2810	0.01	0.356	0.004	0.0480	0.0005	0.0539	0.0006	0.95	310	302	367	25	82
3c	110	2469	0.03	0.443	0.005	0.0570	0.0006	0.0563	0.0006	0.94	372	358	463	24	77
4.1c	102	988	0.85	1.028	0.012	0.1039	0.0011	0.0718	0.0008	0.94	718	637	979	22	65
4.2c	99	2374	0.02	0.438	0.005	0.0527	0.0006	0.0603	0.0007	0.94	369	331	613	24	54
6.1c	10	90	0.50	1.151	0.017	0.1255	0.0014	0.0665	0.0009	0.78	778	762	823	29	93
6.2c	15	212	0.17	0.723	0.010	0.0891	0.0010	0.0588	0.0008	0.84	552	550	561	27	98
7.2c	73	1834	0.02	0.387	0.005	0.0520	0.0006	0.0540	0.0006	0.92	332	327	371	25	88
8.1c	62	501	0.44	1.378	0.016	0.1413	0.0016	0.0708	0.0008	0.92	880	852	950	23	90
8.2c	29	317	0.20	0.958	0.012	0.1107	0.0012	0.0627	0.0008	0.88	682	677	699	25	97
10c	61	834	0.22	0.746	0.009	0.0880	0.0010	0.0615	0.0007	0.92	566	544	655	24	83
11.1c	7	87	0.78	0.691	0.012	0.0845	0.0010	0.0593	0.0010	0.69	533	523	579	36	90
11.2c	98	1572	0.05	0.635	0.008	0.0801	0.0009	0.0575	0.0006	0.93	499	497	511	24	97
12.1c	19	325	0.19	0.569	0.008	0.0719	0.0008	0.0574	0.0007	0.85	457	448	506	28	89
12.2c	157	4467	0.11	0.348	0.004	0.0454	0.0005	0.0557	0.0006	0.93	303	286	439	24	65
13c	46	1043	0.03	0.430	0.005	0.0568	0.0006	0.0550	0.0006	0.90	364	356	411	26	87
14.2c	87	2249	0.02	0.377	0.005	0.0504	0.0006	0.0542	0.0006	0.90	325	317	380	26	83
15c	67	1133	0.07	0.607	0.008	0.0760	0.0009	0.0579	0.0007	0.89	481	472	525	26	90
16.2c	86	1453	0.04	0.592	0.007	0.0762	0.0009	0.0564	0.0007	0.90	472	474	466	26	102
17c	106	1769	0.05	0.620	0.008	0.0773	0.0009	0.0582	0.0007	0.91	490	480	535	26	90
18c	75	1739	0.02	0.427	0.005	0.0563	0.0006	0.0550	0.0007	0.88	361	353	411	27	86
19c	117	2052	0.07	0.580	0.007	0.0734	0.0008	0.0573	0.0007	0.91	465	457	504	25	91
20c	72	1135	0.05	0.666	0.008	0.0817	0.0009	0.0591	0.0007	0.89	518	506	570	25	89
22c	74	1972	0.03	0.381	0.005	0.0486	0.0005	0.0568	0.0007	0.87	328	306	483	27	63
23c	99	1573	0.07	0.639	0.008	0.0808	0.0009	0.0574	0.0007	0.90	502	501	507	26	99
24c	102	1656	0.05	0.628	0.008	0.0798	0.0009	0.0571	0.0007	0.90	495	495	495	26	100
25c	112	2013	0.05	0.577	0.007	0.0711	0.0008	0.0589	0.0007	0.89	463	443	562	26	79
26c	94	1728	0.04	0.544	0.007	0.0702	0.0008	0.0562	0.0007	0.88	441	438	459	27	95
27c	133	2301	0.04	0.591	0.007	0.0753	0.0009	0.0570	0.0007	0.89	472	468	490	27	96
28c	114	1701	0.08	0.687	0.009	0.0861	0.0010	0.0579	0.0007	0.88	531	532	527	27	101
29c	96	1801	0.06	0.540	0.007	0.0689	0.0008	0.0568	0.0007	0.88	438	430	482	27	89
30c	95	1818	0.06	0.525	0.007	0.0677	0.0008	0.0562	0.0007	0.87	428	422	460	28	92
ES 8 La Salvetat Migmatite															
1.1d	33	892	0.01	0.351	0.004	0.0478	0.0005	0.0532	0.0006	0.88	305	301	337	27	89
1.2d	18	156	2.20	0.766	0.011	0.0932	0.0011	0.0596	0.0008	0.79	578	575	590	30	97
2.1d	27	184	0.80	1.447	0.018	0.1533	0.0017	0.0685	0.0008	0.88	909	919	882	25	104
2.2d	82	828	1.03	0.812	0.010	0.0995	0.0011	0.0592	0.0007	0.93	604	611	575	24	106
3d	44	497	0.33	0.867	0.011	0.1047	0.0012	0.0601	0.0007	0.91	634	642	607	25	106
4d	25	631	0.01	0.389	0.006	0.0504	0.0006	0.0560	0.0009	0.69	334	317	451	36	70
5d	52	353	0.93	1.480	0.019	0.1512	0.0017	0.0710	0.0009	0.88	922	908	957	25	95
6d	26	341	0.29	0.753	0.010	0.0886	0.0010	0.0616	0.0008	0.86	570	547	661	27	83
7d	67	635	1.41	0.839	0.011	0.0983	0.0011	0.0619	0.0008	0.86	619	605	670	27	90
8d	61	644	0.72	0.817	0.010	0.1014	0.0011	0.0585	0.0007	0.90	607	623	547	26	114
9d	25	194	0.99	1.141	0.016	0.1276	0.0014	0.0648	0.0009	0.83	773	774	768	28	101
10d	55	429	0.36	1.413	0.017	0.1496	0.0017	0.0685	0.0008	0.91	894	899	884	24	102
11d	10	81	0.52	1.306	0.020	0.1414	0.0016	0.0670	0.0010	0.74	848	853	838	32	102
12d	116	764	0.11	2.616	0.032	0.1827	0.0020	0.1039	0.0012	0.91	1305	1082	1694	21	64
13d	201	2497	0.17	0.830	0.010	0.0990	0.0011	0.0608	0.0007	0.93	614	608	633	24	96
14d	71	605	0.12	1.370	0.018	0.1463	0.0016	0.0679	0.0008	0.88	876	880	866	25	102
15d	89	752	0.16	1.366	0.017	0.1454	0.0016	0.0681	0.0008	0.89	875	875	873	24	100
16.1d	29	413	0.09	0.713	0.010	0.0872	0.0010	0.0593	0.0008	0.78	547	539	578	30	93
16.2d	43	172	2.04	2.044	0.027	0.2038	0.0023	0.0728	0.0009	0.86	1130	1195	1007	25	119
17d	40	255	0.73	1.693	0.023	0.1685	0.0019	0.0729	0.0010	0.83	1006	1004	1010	26	99
18d	59	627	0.18	1.002	0.013	0.1162	0.0013	0.0625	0.0008	0.87	705	709	692	26	102
19d	36	516	0.53	0.653	0.010	0.0779	0.0009	0.0608	0.0009	0.74	511	484	632	33	77
20d	94	1132	0.29	0.824	0.011	0.0990	0.0011	0.0604	0.0007	0.87	611	608	619	26	98
21d	53	597	0.50	0.852	0.011	0.1020	0.0012	0.0606	0.0008	0.87	626	626	627	27	100
22d	295	653	0.48	11.792	0.149	0.4746	0.0053	0.1802	0.0022	0.89	2588	2504	2655	20	94
23.1d	10	98	0.26	1.049	0.016	0.1205	0.0014	0.0631	0.0010	0.75	728	734	713	32	103
23.2d	19	215	0.22	0.942	0.014	0.1084	0.0012	0.0630	0.0009	0.78	674	663	709	30	94
24d	93	1001	0.69	0.927	0.012	0.0977	0.0011	0.0688	0.0009	0.84	666	601	894	26	67
25d	31	352	0.69	0.764	0.011	0.0930	0.0011	0.0596	0.0008	0.81	576	573	588	29	98
26d	113	653	0.28	2.378	0.031	0.2036	0.0023	0.0847	0.0011	0.86	1236	1195	1309	24	91
27d	176	360	0.63	13.005	0.171	0.4959	0.0056	0.1902	0.0024	0.86	2680	2596	2744	20	95
28d	13	138	0.53	0.867	0.014	0.1026	0.0012	0.0613	0.0010	0.73	634	630	649	33	97

grain	[Pb]	[U]	[Th]	Th/U	206 Pb/	±	207 Pb/	±	208 Pb/	±	Ages			
	(ppm)	(ppm)	(ppm)		238 U	(1σ)	235 U	(1σ)	232 Th	(1σ)	206 Pb/	207 Pb/	208 Pb/	±
											238 U	235 U	232 Th	(1σ)
ES7 Laouzas Granite														
33a	1405	14522	72329	5	0.0459	0.0006	0.3167	0.0045	0.0143	0.0002	289	279	287	3
34a	1331	8983	82279	9	0.0463	0.0006	0.3171	0.0046	0.0142	0.0002	292	280	284	3
35a	1561	13906	84806	6	0.0469	0.0006	0.3241	0.0046	0.0144	0.0002	296	285	289	3
36a	1255	5650	86272	15	0.0464	0.0006	0.3174	0.0050	0.0140	0.0002	292	280	282	3
37a	1526	7457	102172	14	0.0469	0.0006	0.3195	0.0048	0.0141	0.0002	295	282	284	3
38a	1422	6446	95482	15	0.0471	0.0006	0.3250	0.0050	0.0143	0.0002	296	286	287	3
39a	1223	9071	72384	8	0.0464	0.0006	0.3141	0.0046	0.0143	0.0002	293	277	287	3
40a	1316	6291	88790	14	0.0464	0.0006	0.3234	0.0050	0.0141	0.0002	292	285	283	3
41a	1869	5871	110726	19	0.0510	0.0006	0.3636	0.0064	0.0169	0.0002	321	315	339	4
42a	1664	7306	95010	13	0.0511	0.0006	0.3540	0.0056	0.0166	0.0002	321	308	332	4
43a	1427	5587	83966	15	0.0506	0.0006	0.3511	0.0057	0.0165	0.0002	318	306	330	4
44a	1505	6351	89387	14	0.0503	0.0006	0.3457	0.0056	0.0161	0.0002	316	302	323	3
45a	1421	3511	87118	25	0.0515	0.0007	0.3737	0.0068	0.0168	0.0002	324	322	337	4
46a	1467	8153	80517	10	0.0504	0.0006	0.3488	0.0053	0.0163	0.0002	317	304	328	4
47a	1385	12594	62010	5	0.0505	0.0006	0.3437	0.0050	0.0166	0.0002	317	300	332	4
48a	1402	13808	60267	4	0.0506	0.0006	0.3464	0.0050	0.0164	0.0002	318	302	330	4
50a	1343	12757	60159	5	0.0507	0.0006	0.3468	0.0051	0.0161	0.0002	319	302	322	3
51a	1254	5577	75446	14	0.0514	0.0006	0.3570	0.0058	0.0156	0.0002	323	310	313	3
52a	1210	10014	56262	6	0.0506	0.0006	0.3483	0.0051	0.0166	0.0002	319	304	333	4
53a	1279	11628	59034	5	0.0506	0.0006	0.3470	0.0051	0.0160	0.0002	318	302	320	3
54a	1275	4595	79000	17	0.0520	0.0006	0.3656	0.0063	0.0157	0.0002	327	316	315	3
55a	864	3086	52825	17	0.0513	0.0006	0.3551	0.0065	0.0160	0.0002	323	309	320	3
56a	1224	5645	70387	12	0.0510	0.0006	0.3458	0.0053	0.0162	0.0002	321	302	324	3
57a	1238	7421	68419	9	0.0510	0.0006	0.3418	0.0054	0.0157	0.0002	320	299	315	3
58a	1312	5427	74832	14	0.0522	0.0006	0.3527	0.0056	0.0166	0.0002	328	307	333	4
59a	1003	6587	54512	8	0.0504	0.0006	0.3473	0.0057	0.0156	0.0002	317	303	312	3
60a	1107	6681	62592	9	0.0502	0.0006	0.3376	0.0057	0.0154	0.0002	316	295	309	3
61a	1453	10545	74983	7	0.0499	0.0006	0.3476	0.0053	0.0158	0.0002	314	303	318	3
62a	1050	5823	58804	10	0.0506	0.0006	0.3544	0.0057	0.0158	0.0002	318	308	318	3
63a	1061	3078	66792	22	0.0509	0.0006	0.3549	0.0065	0.0159	0.0002	320	308	319	3
64a	1212	12417	52947	4	0.0497	0.0006	0.3419	0.0050	0.0158	0.0002	313	299	316	3
Mz1.1 (fsp)	346	3072	14349	5	0.0506	0.0007	0.5039	0.0078	0.0167	0.0002	318	414	335	4
Mz1.2 (fsp)	1015	7710	50744	7	0.0473	0.0006	0.3374	0.0048	0.0154	0.0002	298	295	309	4
Mz2.1 (crd)	1072	8419	51320	6	0.0489	0.0007	0.3815	0.0055	0.0157	0.0002	308	328	315	4
Mz2.2 (crd)	1218	7907	57072	7	0.0519	0.0007	0.3798	0.0054	0.0169	0.0002	326	327	338	4
Mz3.1 (qtz)	1372	10036	73905	7	0.0458	0.0006	0.3173	0.0045	0.0148	0.0002	289	280	296	4
Mz3.2 (qtz)	1444	10503	79124	8	0.0460	0.0006	0.3171	0.0045	0.0145	0.0002	290	280	292	4
Mz4.1 (fsp)	1373	1157	55048	48	0.0460	0.0006	0.3170	0.0046	0.0148	0.0002	290	280	297	4
Mz4.2 (fsp)	1423	1206	56888	47	0.0462	0.0006	0.3264	0.0049	0.0149	0.0002	291	287	299	4
Mz5 (qtz)	880	732	35685	49	0.0576	0.0008	0.4697	0.0089	0.0195	0.0003	361	391	390	5
Mz6 (qtz)	1247	1045	50170	48	0.0508	0.0007	0.3525	0.0053	0.0175	0.0002	319	307	350	4
Mz7 (qtz)	1396	10994	73918	7	0.0474	0.0007	0.3261	0.0050	0.0157	0.0002	298	287	314	4
Mz8 (qtz)	713	5795	37073	6	0.0462	0.0007	0.3156	0.0049	0.0148	0.0002	291	279	298	4
Mz9.1 (fsp)	667	7610	33851	4	0.0478	0.0007	0.3389	0.0054	0.0152	0.0002	301	296	305	4
Mz9.2 (fsp)	136	1285	4509	4	0.0565	0.0008	0.3988	0.0065	0.0198	0.0003	354	341	396	5
Mz10.1 (qtz)	1305	6046	81834	14	0.0465	0.0007	0.4293	0.0069	0.0148	0.0002	293	363	297	4
Mz10.2 (qtz)	1318	8843	61053	7	0.0469	0.0007	0.3484	0.0057	0.0151	0.0002	295	304	303	4
Mz10.3 (qtz)	1344	10119	76298	8	0.0491	0.0007	0.3752	0.0062	0.0153	0.0002	309	324	306	4
Mz11.1 (qtz-j)	1121	8693	56704	7	0.0466	0.0007	0.3239	0.0054	0.0148	0.0002	294	285	298	4
Mz11.2(qtz-j)	1359	1165	55336	48	0.0474	0.0007	0.3382	0.0056	0.0152	0.0002	298	296	304	4

grain	[Pb]	[U]	[Th]	Th/U	206 Pb/	±	207 Pb/	±	208 Pb/	±	Ages			
	(ppm)	(ppm)	(ppm)		238 U	(1σ)	235 U	(1σ)	232 Th	(1σ)	206 Pb/ 238 U	207 Pb/ 235 U	208 Pb/ 232 Th	± (1σ)
ES8 La Salvetat Migmatite														
65a	1230	5483	67669	12	0.0518	0.0006	0.3603	0.0058	0.0163	0.0002	326	312	327	3
66a	1189	18268	32530	2	0.0496	0.0006	0.3407	0.0050	0.0160	0.0002	312	298	321	3
67a	853	8595	34736	4	0.0511	0.0006	0.3507	0.0054	0.0160	0.0002	321	305	321	3
68a	942	12580	30216	2	0.0502	0.0006	0.3479	0.0052	0.0161	0.0002	316	303	324	3
69a	730	7226	30260	4	0.0510	0.0006	0.3552	0.0055	0.0159	0.0002	321	309	319	3
70a	1097	16108	32500	2	0.0496	0.0006	0.3411	0.0051	0.0157	0.0002	312	298	315	3
71a	854	10883	27100	2	0.0522	0.0006	0.3715	0.0056	0.0164	0.0002	328	321	328	3
72a	1543	25307	37012	1	0.0502	0.0006	0.3449	0.0050	0.0160	0.0002	316	301	321	3
73a	1307	19895	34723	2	0.0504	0.0006	0.3497	0.0052	0.0162	0.0002	317	305	325	3
74a	1229	18313	34893	2	0.0499	0.0006	0.3445	0.0051	0.0159	0.0002	314	301	318	3
75a	1571	25306	37535	1	0.0508	0.0006	0.3528	0.0052	0.0161	0.0002	319	307	324	3
76a	781	8381	31410	4	0.0501	0.0006	0.3488	0.0055	0.0156	0.0002	315	304	313	3
77a	No data due to a « bug » with Glitter.				0.0500	0.0006	0.3426	0.0052	0.0158	0.0002	314	299	317	3
78.1a					0.0503	0.0006	0.3496	0.0052	0.0161	0.0002	317	304	322	3
78.2a					0.0505	0.0006	0.3483	0.0052	0.0162	0.0002	317	303	325	3
78.3a					0.0510	0.0006	0.3529	0.0055	0.0159	0.0002	321	307	318	3
79a					0.0485	0.0006	0.3352	0.0053	0.0150	0.0002	305	294	300	3
80.1a					0.0475	0.0006	0.3316	0.0052	0.0147	0.0002	299	291	295	3
80.2a					0.0475	0.0006	0.3375	0.0053	0.0149	0.0002	299	295	298	3
81.1a					0.0474	0.0006	0.3294	0.0050	0.0150	0.0002	299	289	300	3
81.2a					0.0467	0.0006	0.3245	0.0049	0.0148	0.0002	294	285	296	3
82a					0.0466	0.0006	0.3221	0.0049	0.0147	0.0002	294	284	296	3
83a	0.0477	0.0006	0.3292	0.0052	0.0147	0.0002	300	289	294	3				
84a	0.0469	0.0006	0.3236	0.0049	0.0148	0.0002	295	285	297	3				
2b	713	6409	34056	5	0.0483	0.0006	0.3501	0.0062	0.0152	0.0002	304	305	306	3
3.1b	929	9780	40809	4	0.0480	0.0006	0.3415	0.0059	0.0150	0.0002	302	298	301	3
3.2b	772	5903	39878	7	0.0481	0.0006	0.3461	0.0063	0.0150	0.0002	303	302	301	3
3.3b	890	7957	42165	5	0.0484	0.0006	0.3458	0.0061	0.0150	0.0002	305	302	301	3
4b	869	8361	39428	5	0.0483	0.0006	0.3421	0.0062	0.0149	0.0002	304	299	300	3
5.2b	924	10015	39179	4	0.0474	0.0006	0.3393	0.0062	0.0147	0.0002	299	297	295	3
6b	676	6290	32046	5	0.0472	0.0006	0.3230	0.0063	0.0142	0.0002	297	284	285	3
7b	1186	19504	31251	2	0.0472	0.0006	0.3296	0.0062	0.0145	0.0002	297	289	291	3
8.1b	1213	17656	38626	2	0.0468	0.0006	0.3330	0.0064	0.0143	0.0002	295	292	288	3
8.2b	1300	20670	37530	2	0.0462	0.0006	0.3263	0.0063	0.0141	0.0001	291	287	283	3
9b	1738	32151	38690	1	0.0455	0.0006	0.3196	0.0063	0.0141	0.0001	287	282	282	3
10b	1074	16844	30899	2	0.0464	0.0006	0.3196	0.0065	0.0141	0.0001	292	282	283	3
11b	1481	24419	39221	2	0.0461	0.0006	0.3241	0.0066	0.0141	0.0001	291	285	283	3
12b	784	7353	35558	5	0.0474	0.0006	0.3314	0.0073	0.0140	0.0001	299	291	280	3
Mz12 (qtz)	731	9662	27745	3	0.0465	0.0006	0.3554	0.0054	0.0142	0.0002	293	309	285	3
Mz13 (qtz)	973	11793	39613	3	0.0455	0.0006	0.3248	0.0047	0.0146	0.0002	287	286	294	3
Mz15 (bt)	137	1909	5184	3	0.0447	0.0006	0.3430	0.0067	0.0142	0.0002	282	300	285	3
Mz17 (bt)	838	11024	30254	3	0.0454	0.0006	0.3177	0.0048	0.0149	0.0002	286	280	300	3
Mz20 (bt)	735	8040	29039	4	0.0474	0.0006	0.3310	0.0053	0.0156	0.0002	299	290	312	4
Mz21.1 (bt)	1007	12699	36732	3	0.0495	0.0006	0.3700	0.0059	0.0155	0.0002	311	319	311	4
Mz21.2 (bt)	1138	12832	44059	3	0.0450	0.0006	0.3459	0.0067	0.0150	0.0002	284	302	300	4
Mz23 (bt)	463	4871	15302	3	0.0468	0.0006	0.4067	0.0071	0.0147	0.0002	295	346	295	3